ISSN 2543-9901

JOURNAL OF CASTING & MATERIALS ENGINEERING

AGH UNIVERSITY OF KRAKOW
FACULTY OF FOUNDRY ENGINEERING

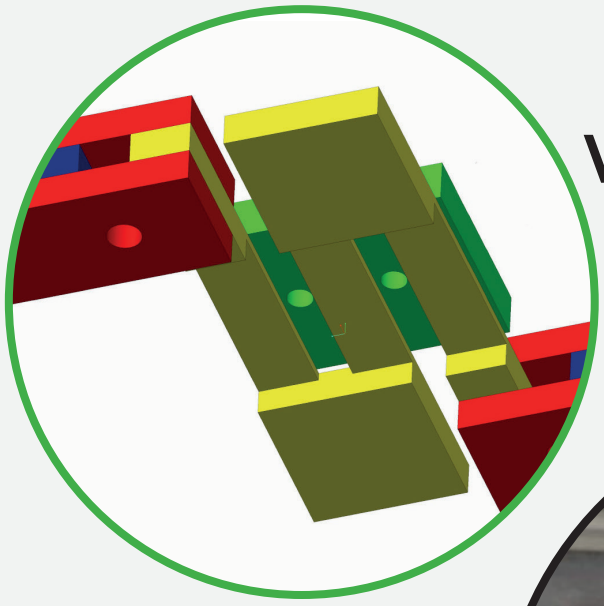

QUARTERLY
Vol. 10 No. 1/2026

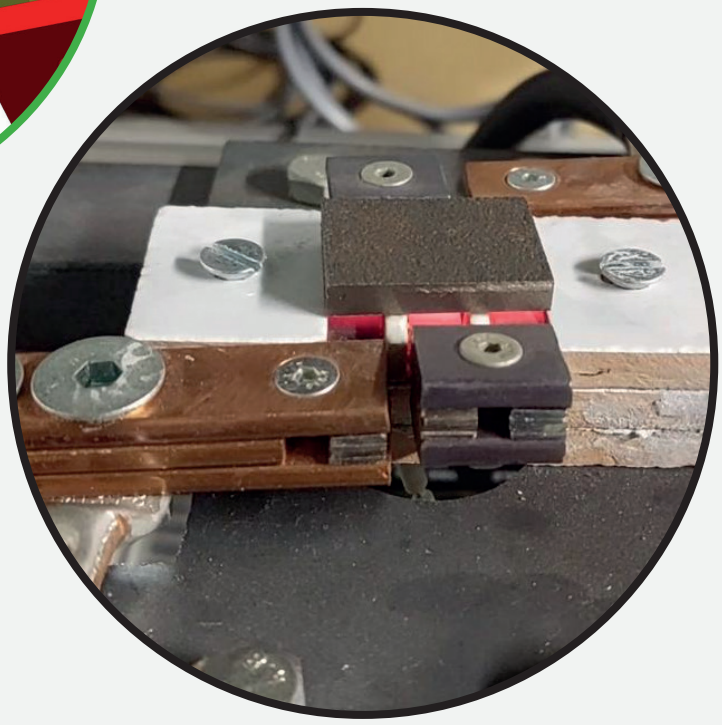

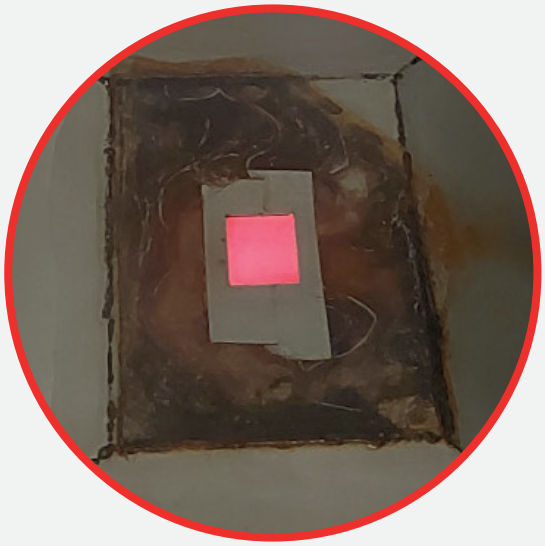

JCME

AGH UNIVERSITY PRESS
KRAKOW 2026

www:
https://journals.agh.edu.pl/jcme/

AGH UNIVERSITY PRESS KRAKOW 2026

Wydawnictwa AGH (AGH University Press)
al. A. Mickiewicza 30, 30-059 Kraków
tel. 12 617 32 28, 12 638 40 38
e-mail: redakcja@wydawnictwoagh.pl
http://www.wydawnictwa.agh.edu.pl

Contents

Journal of Casting & Materials Engineering Vol. 10 No. 1 (2026) 1–9
https://doi.org/10.7494/jcme.2026.10.1.1-9

The Influence of Modified Inorganic Binders Intended for 3D Printing on Selected Properties of Thermally Cured Moulding Sands – Conventionally and with Microwaves

Dawid M. Halejcio[a], Katarzyna Major-Gabryś[a*]

[a] AGH University of Krakow, Faculty of Foundry Engineering, 30 Mickiewicza Av., 30-059 Krakow, Poland
[*] *email: katmg@agh.edu.pl*

Received: 3 March 2026/Accepted: 23 March 2026/Published online: 31 March 2026.
This article is published with open access at AGH University of Science and Technology Journals.

Abstract

This study determined the impact of thermal curing on the basic properties of moulding compounds made with commercial inorganic binders and binders based on them, modified for use in 3D printing technology (Binder Jetting). Two inorganic binders based on sodium silicate and a binder based on aluminosilicates were tested. As part of the work, the parameters for thermal curing of the mixtures were selected: for curing in a dryer, the best properties were obtained for mixtures containing 2.0 p.p.w. of binder cured for 10 min at 160°C. In the case of microwave curing, the best properties were obtained for moulding sands containing 2.0 p.p.w. of binder cured for 6 min at a device power of 800 W. The tests showed that the basic properties of moulding compounds with binders developed on the basis of commercial binders for use in 3D printing technology, thermally cured in a dryer, do not differ significantly from the properties of compounds with commercial binders. In the case of microwave curing, a reduction in the strength of compounds with new binders was observed in relation to compounds with classic binders. Thermal deformation tests of compounds with classic and modified binders confirmed the typical behavior observed for inorganic systems. It was proven that new, modified inorganic binders developed for 3D printing of moulds and cores using Binder Jetting technology can be used as binding materials in thermally cured moulding sands. Both thermal curing methods were assessed as suitable for curing moulding compounds with new binders.

Keywords:

moulding sands, sand 3D printing, inorganic binders, thermal curing, microwaves

1. INTRODUCTION

Strict environmental protection requirements have led to intensive work over the last few decades to develop environmentally friendly moulding sands with inorganic binding systems as an alternative to organic-bonded sands. These changes are currently being implemented in foundry practice, but the use of organic binders is still predominant in the production of castings in disposable moulds made of II generation moulding sands (bonded with binders) and in moulds using cores made of II generation compounds. This is the reason justifying further development of inorganic systems and the possibilities of adapting them for modern technologies aligned with Foundry 4.0 assumptions, such as additive manufacturing.

In foundry moulding sands, three main types of inorganic binders are used: sodium silicates, phosphate-based binders, and geopolymer binders. Sodium silicate binders are commonly used in foundry practice due to their good water solubility, compliance with environmental standards, and ability to achieve adequate mechanical strength through the curing process [1–3]. Geopolymer binders, known as inorganic polymers, are aluminosilicate materials. Their potential for use in foundry practice stems mainly from their natural origin and their ability to undergo controlled polymerization of aluminosilicate monomers [4, 5]. Compounds with phosphate binders are not currently used in foundry practice and are not the subject of research conducted as part of this work.

Curing (dehydration) of compounds with inorganic binders can be carried out at ambient temperature by using curing agents (chemical curing) – self-curing moulding sands (ester curing agents), and CO_2 degassing of moulds and cores, as well as at elevated temperatures (physical curing) – conventional thermal curing and microwave curing. The choice of moulding sand's hardening technology directly affects the properties of the moulds and cores made from them and may indirectly affect the quality of the castings obtained. Unlike chemical curing, thermal curing allows the binder to be cured by controlled temperature increase, which results in water evaporation and the formation of strong bonds that bind the sand matrix grains. The strength of thermally cured hydrated sodium silicate mixture is approximately 10 times higher than that of chemically cured mixtures with a similar composition. Table 1 compares the effect of the curing method of hydrated sodium silicate sands on their strengths [1, 2].

Table 1
Comparison of compressive strength obtained for hydrated sodium silicate sands prepared using different curing technologies [1, 2]

Moulding sands' components, amount, p.p.w.	Curing technology	Compressive strength, MPa
Quartz sand, 100 Hydrated sodium silicate (M = 2.2), 4.0	thermal (physical)	10.0–11.0
	CO_2 (chemical)	1.0–1.2
	ester/4 h (chemical)	0.8–1.3

The differences in moulding sands' strength values are caused by different mechanisms of water removal from the binding systems, as shown in Figure 1 [3, 4].

Chemical hardening, which occurs in the case of ester technology and CO_2 gassing technology, causes slow dehydration of the moulding sand – the time required to completely remove water from the binder can be as long as 24 hours (Fig. 1a). Convection drying (Fig. 1b), which depends on the thermal conductivity of the moulding sand, is a process in which water is gradually removed from successive layers of the sand during heating. Due to energy losses during heating, mainly related to the efficiency of drying equipment and the method of heat transfer, convection drying is a time-consuming and energy-intensive process. In the traditional thermal hardening method, a temperature range of 140°C to 180°C is used [6]. In the case of hydrated sodium silicate-based binders, the curing process consists of several distinct phases: elimination of free water, removal of bound water, and formation of silicate bridges as the result of dehydration reactions. The energy transfer mechanism is mainly based on conduction, which means that heating starts at the surface and gradually progresses into the material [7]. The use of heat accelerates the evaporation of water from the binder solution, which leads to an increase in viscosity and promotes the formation of stable bridges between sand grains [1, 8]. Microwave curing, which provides a different means of energy transfer than traditional heating methods (Fig. 1c), may be more efficient in the curing process of moulding sands with hydrated sodium silicate. Electromagnetic radiation at a frequency of 2.45 GHz rapidly heats the moulding sand by rotating water molecules, resulting in faster and more uniform temperature distribution throughout the material. Through high-frequency vibrations, the energy of the electromagnetic wave is converted into the thermal energy of the binder, intensifying the process of forming a dehydrated layer of glassy sodium silicate. This mechanism significantly reduces the curing time and can also improve the quality of the bonds between sand grains. The microwave curing process combines the advantages of traditional curing methods, such as process speed and reduction in binder quantity, while maintaining good mechanical and technological properties. The higher strength of the moulding sand allows for a reduction in wall thickness or a reduction in the volume of large cores. This can result in a reduction in the amount of sand used, and thus a reduction in production costs and an improvement in knockout efficiency. In addition, during hardening, the moulding sand is heated to lower temperatures (even twice as low) compared to conventional methods [5, 6]. The higher strength of the sand also allows for a reduction in the amount of binder in the sand, which has a positive effect on knockout and mechanical regeneration, i.e., the properties of silicate-bonded sands, which are well known to pose a technological challenge [1].

Geopolymer binders, similarly to sodium silicate-based binders, can be cured chemically and thermally. After adding the hardener, polymerization and gelation (cross-linking) occur, resulting in the formation of an inorganic polymer that binds the sand matrix grains [9]. During thermal curing, the binder also undergoes polymerization, leading to the formation of three-dimensional aluminosilicate networks (N-A-S-H gels, C-A-S-H gels) – the formation of an inorganic polymer with appropriate mechanical properties and stability [10, 11].

When comparing the presented physical curing methods, it should be noted that thermal curing requires heating the entire working chamber of the furnace, which is associated with significant energy losses to the environment and high unit energy consumption, especially in the production of large-size moulds [12]. In the case of microwave curing, during which energy is selectively supplied to the material, mainly to the water contained in the binder, it is possible to shorten the process time and reduce unit costs, despite losses associated with the conversion of electricity into microwaves [13, 14].

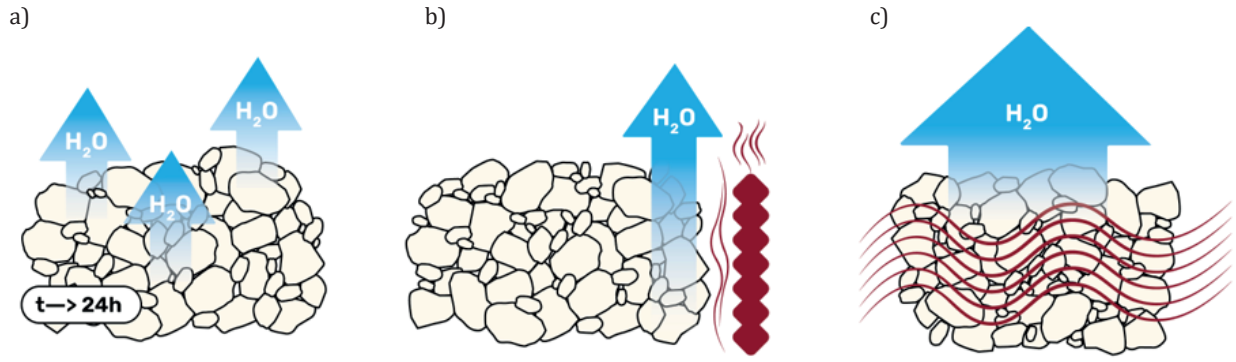

Fig. 1. Schematic diagrams of water removal during the curing of moulding sands with hydrated sodium silicate: a) using chemical methods; b) by heating in a convector; c) by microwave curing [3, 4]

Currently, in foundry practice, conventional or microwave thermal hardening of moulds and cores made using Binder Jetting technology is not used. However, these processes are used in the production of ceramic printed components ($BaTiO_3$, $CaSO_4 \cdot ½H_2O$), in which postprocess thermal treatment (heating, firing) is necessary to give the finished components the desired properties [15, 16]. Considering the benefits of the thermal curing of moulding compounds, it seems entirely justified to conduct research on the development of moulding compounds with thermally cured inorganic binders intended for 3D printing of sand moulds and cores. Furthermore, 3D printing of sand moulds using inorganic binders is an advanced and forward-looking technology that ensures high dimensional accuracy, repeatability, and process efficiency, making it an excellent solution for modern foundry engineering.

Binders used in Binder Jetting technology should ensure the highest possible print quality. One of the key parameters is the appropriate viscosity of the binder, which allows for its precise jetting using a print head. Another important aspect is the degree to which the substrate layers are saturated with the binder. Under ideal conditions, the binder should cover only a single layer of the substrate; however, in practice, the drop spreads across the material grains, and its excess penetrates deeper into the substrate. This is the reason for the varying properties observed across different cross-sections in the printed parts. The final important parameter is the interaction between the binder and the substrate. The binder used should be selected to suit the material so that it adequately wets the substrate, allowing a thin layer to form on the surface of the grains and subsequently enabling the formation of bonding bridges [17–20].

2. OWN RESEARCH

As part of this work, moulding compounds with thermally cured inorganic binders were tested. Three commercial binders (A, B, C) and their equivalents developed for 3D printing Binder Jetting technology were used [12, 13]. In the first stage of the research the curing process parameters were selected. Then, the influence of the binder type on selected properties of the compounds was determined. The aim of this article is to evaluate selected properties of molding compounds containing modified inorganic binders, designed for Binder Jetting technology, which are thermally cured using both conventional heating (drying) and microwave treatment. The study includes a comparison of test results obtained for molding sands using commercially available binders and their counterparts modified for 3D printing. As part of the study, an analysis of the effect of curing parameters on selected properties of the mixtures was also conducted.

2.1. Selection of process parameters

Moulding compounds intended for microwave curing were prepared using a paddle mixer, in which the matrix and binder were mixed for 60 s. Standard test specimens were compacted by vibration using a WADAP LUZ device (vibration time 9 s). The moulding sands were cured in an 800 W microwave oven at a frequency of 2.45 GHz. Both the amount of binder and then the curing time (for moulding sand A binder – 2.0 p.p.w.) were selected. The strength of the compounds was determined within a curing time range of 3–8 min. Figure 2 shows the research results. It has been demonstrated that compounds cured by microwaves for 3 min exhibit good strength properties from the perspective of foundry practice and extending the time of curing improves it. On the other hand, extending the curing time results in higher energy consumption. Therefore, it is necessary to select process parameters that meet production requirements. Based on the results obtained, the following parameters were selected as optimal for microwave hardened compounds: a curing time of 6 min and 2.0 p.p.w. of binder.

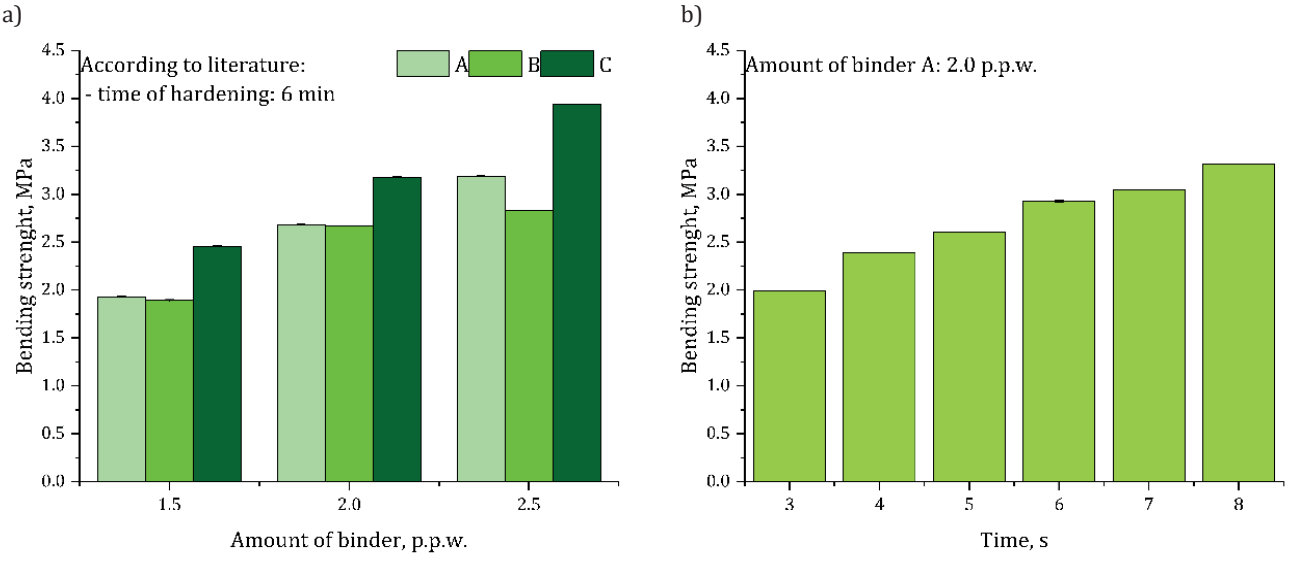

Fig. 2. Selection of parameters of the microwave curing process: a) binder amount; b) time of hardening

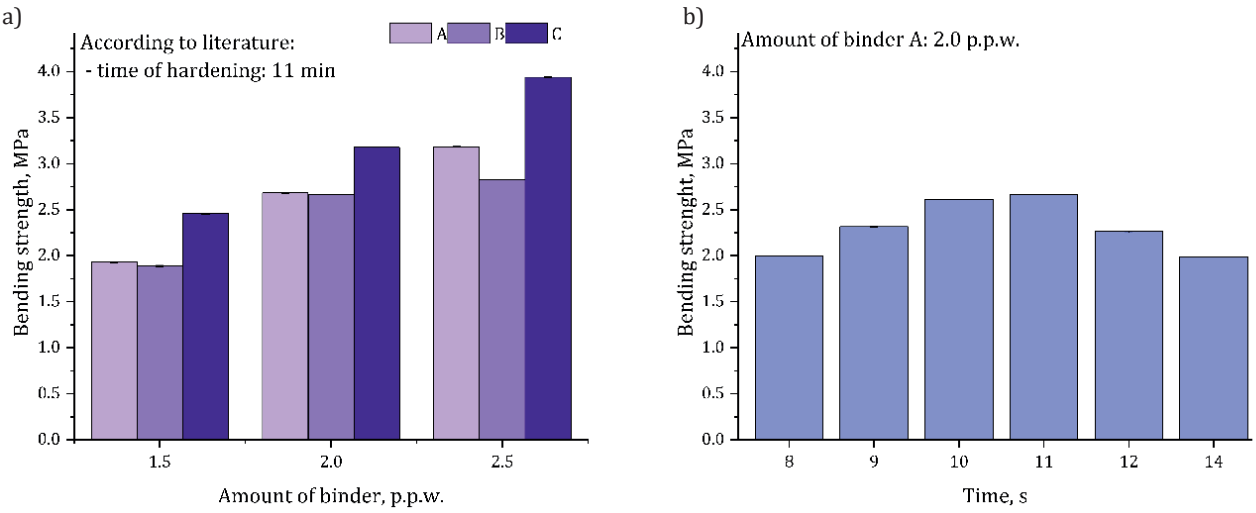

Fig. 3. Selection of parameters of the thermal (in a dryer) curing process: a) binder amount; b) time of hardening

Thermally cured compounds (in a dryer) were prepared in the same way as microwaved cured compounds – in a paddle mixer with a mixing time of 60 s. The moulds were also compacted in the same way as the moulds made of compounds intended for microwave curing – by vibration with a vibration time of 9 s. Curing was carried out in a laboratory dryer at a temperature of 160°C. The selection of the curing time and the amount of binder were also studied (Fig. 3). In order to select the curing time, a moulding compound with 2.0 p.p.w. of binder A was tested, based on its good strength properties. Although a mixture containing 2.5 p.p.w. of binder exhibits better properties, increasing the amount of inorganic binder in the moulding sand results in poorer knockout properties and a reduced capacity for mechanical reclamation. Based on the results presented, a mixture containing 2.0 p.p.w. of binder cured at 160°C for 10 min was selected for further tests of moulding sands thermally hardened in a dryer.

2.2. Materials and methodology

Table 1 presents the compositions of the tested mixtures along with the curing parameters selected on the basis of the tests presented in Section 2.1. The moulding compounds were prepared in a paddle mixer; the mixing time for sand and binder was 60 s. The test specimens (standard: longitudinal, cylindrical, and dog bone standard test specimens) were prepared using a WADAP LUZ vibratory compacting device with vibration time of 9 s. Sibelco quartz sand with a main fraction of 0.20/0.16/0.10 and a main fraction content of 92% was used as the matrix. The standard test specimens were thermally cured according to the method specified in Table 2. A laboratory dryer SA-P-2 (750 W, max temp. around 200°C) was used for conventional thermal curing, and a Whirlpool 800 W microwave oven was used for microwave curing. The binders used were hydrated sodium silicate-based binders (binders A and B) [21, 22] and aluminosilicate binder C [23]. Each of the tested binders underwent physicochemical modification on the basis of Kocel AJS300 3D printer requirements to adapt their parameters for use in 3D printing (A3D, B3D, C3D).

The tests were conducted "cold" – 1 hour after the end of thermal curing. The time was selected experimentally so that the standard test specimens reached ambient temperature throughout their entire volume. The bending and tensile strength tests of the moulding compounds were performed using a universal testing machine (MultiSerw Morek LRu-2e). Permeability was tested using a WADAP LPiR1 apparatus. Standard cylindrical standard test specimens (50 mm × 50 mm) were used to assess apparent density, permeability and friability, while standard-longitudinal standard test specimens (22.36 mm × 22.36 mm × 172 mm) were used to test bending strength. Tensile strength was determined using dog bone standard test specimens with a cross-section of 22.36 mm × 22.36 mm. The abrasion resistance of moulding compounds was tested using a method involving shot falling onto a cylindrical standard test specimen placed in the jaws of an apparatus manufactured by Huta Stalowa Wola. In accordance with the test methodology, steel shot (1.75 kg) with a diameter of approximately 1 mm falls freely from a height of 0.307 m onto a mould rotating at a speed of 1 rpm [24].

The purpose of testing the thermal deformation (by hot distortion parameter) of moulding compounds is to determine the thermal stability of casting cores. When liquid metal is poured into the mould the temperature rises and the metal level rises, leading to intense heating of the cores. The one-sided nature of heating in the initial phase of the process promotes the formation of thermal distortions in the cores, resulting from their expansion and contraction. These phenomena can lead to damage to the cores and the formation of casting defects, affecting its geometry, dimensional accuracy, and surface quality. The hot distortion test was performed using a DMA device manufactured by Multiserw Morek. In accordance with the methodology used, standard test specimens with dimensions of 114 mm × 25.4 mm × 6.3 mm were heated using two halogen lamps with a total power of 500 W to a maximum temperature of 900°C [25, 26].

Table 2
The compositions of the tested moulding sands with the processes curing parameters

Symbol	Matrix, amount, p.p.w.	Binder	Amount of binder, p.p.w.	Method of hardening	Time of hardening, min	Temperature or power
MA1	quartz sand, 100	A*	2.0	in a dryer	10	180°C
MA2		A3D	2.0	in a dryer	10	180°C
MA3		A	2.0	microwave	6	800 W
MA4		A3D	2.0	microwave	6	800 W
MB1		B**	2.0	in a dryer	10	180°C
MB2		B3D	2.0	in a dryer	10	180°C
MB3		B	2.0	microwave	6	800 W
MB4		B3D	2.0	Microwave	6	800 W
MC1		C***	2.0	in a dryer	10	180°C
MC2		C3D	2.0	in a dryer	10	180°C
MC3		C	2.0	microwave	6	800 W
MC4		C3D	2.0	microwave	6	800 W

* A – commercial inorganic binder;
** B – commercial inorganic binder with improved knockout properties;
*** C – commercial inorganic binder based on aluminosilicates;
A3D, B3D, C3D – modified binders elaborated within own research for use in 3D printing technology

2.3. Results and discussion

The results of the tests are presented in Figures 4–10.

Figure 4 shows a comparison of the apparent density of the tested moulding sands. Based on the analysis of the density test results, it was found that the apparent density of thermally hardened moulding sand at 160°C ranges from 1.267 g/cm^3 to 1.376 g/cm^3. The highest density was found for the MC1 mixture (1.376 g/cm^3), while the lowest value was obtained for the MB2 mixture (1.267 g/cm^3) (Fig. 4a). The apparent density of microwave-cured moulding sands ranges from 1.283 g/cm^3 to 1.361 g/cm^3. The highest value was obtained for sand MC3 (1.449 g/cm^3), and the lowest for MB4 (1.283 g/cm^3) (Fig. 4b). In the case of both thermal curing methods, the highest density – the highest degree of compaction – is characteristic of compounds with aluminosilicate binders: a classic one (C) (MC1, MC3) and intended for 3D printing (C3D) (MC2 and MC4).

Figures 5 and 6 show the bending and tensile strength values of the tested moulding sands. Based on the analysis of the bending strength of thermally hardened mixtures using a dryer (Fig. 5a), it can be concluded that the highest results are obtained by moulding mixtures made with sodium silicate binders A and A3D, reaching 2.542 MPa and 2.464 MPa, respectively. For mixtures with modified sodium silicate binder (B) and aluminosilicate binder (C) and their modified equivalents for 3D printing, the strength values do not differ significantly and fluctuate around 2.000 MPa. In the case of microwave-cured sand (Fig. 5b), the obtained bending strength values allow us to conclude that the use of a modified binder for 3D printing leads to a reduction in strength compared to classic binders. The highest value, 3.122 MPa, was achieved for the MC3 compound with binder C. The lowest strength was observed for the MB3 and MB4 compounds, with the MB4 compound using binder B modified for 3D printing, achieving a result 0.582 MPa lower.

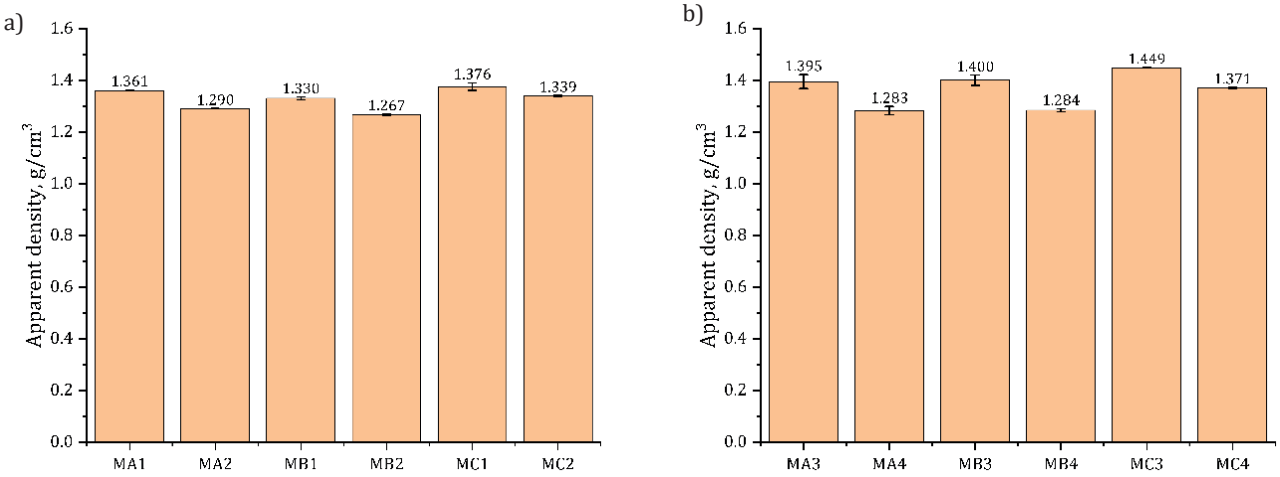

Fig. 4. The influence of binder type on the apparent density of tested moulding sands: a) thermal hardening in a dryer; b) thermal hardening by microwaves

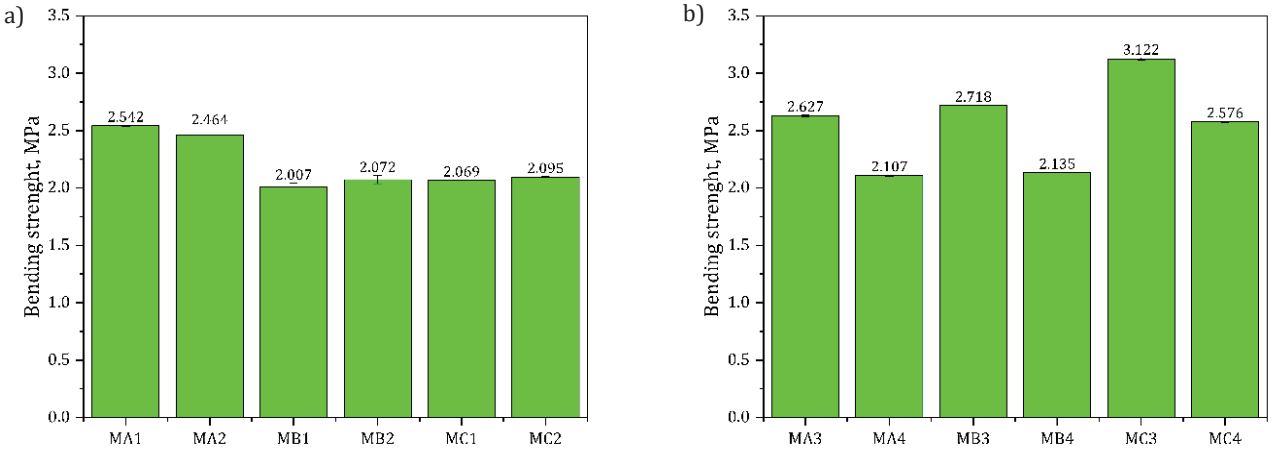

Fig. 5. The influence of binder type on bending strength of tested moulding sands: a) thermal hardening in a dryer; b) thermal hardening by microwaves

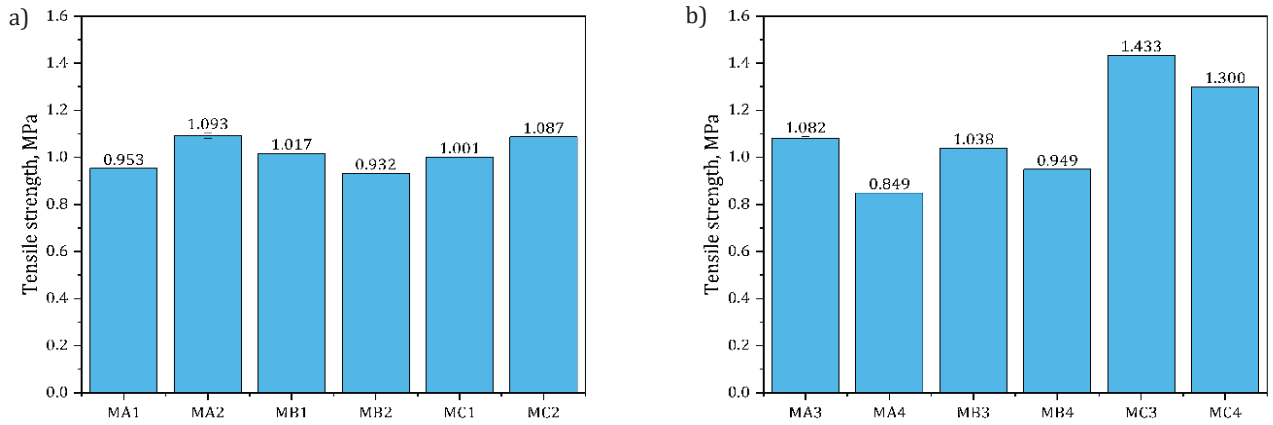

Fig. 6. The influence of binder type on tensile strength of tested moulding sands: a) thermal hardening in a dryer; b) thermal hardening by microwaves

In terms of tensile strength (Fig. 6a), the highest results were obtained for the MA2 compound – 1.093 MPa. This compound is characterized by better tensile strength than its counterpart with a classic binder. In the case of the compound with binder B3D – MB2, a slight decrease in strength was observed compared to its classic counterpart – MB1. In the case of the compound with binder C modified for use in 3D printing (C3D) – MC2, a slight increase in tensile strength was observed compared to the compound with a classic binder – MC2. In the case of microwave-cured mixtures, it was observed that all tested moulding sands using modified binders (MA4, MB4, MC4) are characterized by lower tensile strength values compared to mixtures with classic binders (MA3, MB3, MC3) (Fig. 6b).

Figure 7 shows a comparison of the permeability of the tested moulding sands. Analysis of the obtained test results showed slight differences between the tested moulding compounds thermally cured in a dryer (Fig. 7a). The permeability values range 583.33–608.33 · 10^{-8} m^2/(Pa·s). Mixtures with classic binders, sodium silicate A (MA1) and aluminosilicate C (MC1), are characterized by the best permeability – 608.33 · 10^{-8} m^2/(Pa·s). The lowest permeability value was observed for the mixture with modified sodium silicate binder MB1 – 583.33 · 10^{-8} m^2/(Pa·s). When comparing the permeability values of moulding compounds with a classic binder and one developed for use in 3D printing, it can be seen that the modification of binders does not significantly affect the permeability of the tested compounds. In the case of microwave-cured compounds (Fig. 7b), the permeability values are not significantly higher than in the case of thermal curing in a dryer. The permeability values range 600.00–633.33 · 10^{-8} m^2/(Pa·s). The highest value was obtained for the MA4 mixture with a modified binder (A3D) – 633.33 · 10^{-8} m^2/(Pa·s).

Figure 8 shows a comparison of the friability of the tested moulding compounds. Analysis of the test results showed that thermally cured mixtures in the dryer achieve friability values ranging from 3.007% to 5.328% (Fig. 8a). The lowest friability was observed in the compound with aluminosilicate binder C (MC1) – 3.007%, and the highest in the compound with modified sodium silicate binder B developed for use in 3D printing B3D (MB2) – 5.328%. Modification of commercial binders for use in 3D printing results in the following: in the case of the thermal curing of sands in

a dryer, modified silicate B and aluminosilicate C increases the friability tendency of the tested compounds. As a consequence, this may cause casting defects. Microwave-cured sands are characterized by similar friability in the range of 4.453–4.594% (Fig. 8b). The differences in friability values between compounds made with classic binders (MA3, MB3, MC3) and compounds made with binders developed for 3D printing (MA4, MB4, MC4) are minimal and do not exceed 0.150 percentage point.

Figures 9 and 10 show the effect of the type of binder used on the thermal deformation of the tested compounds, determined on the basis of the hot distortion parameter tests.

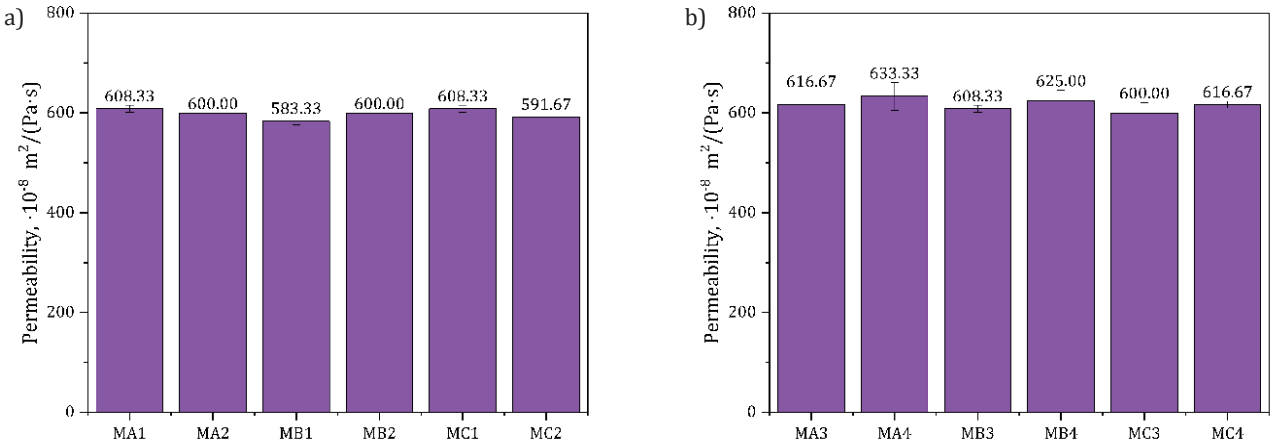

Fig. 7. The influence of binder type on permeability of tested moulding sands: a) thermal hardening in a dryer; b) thermal hardening by microwaves

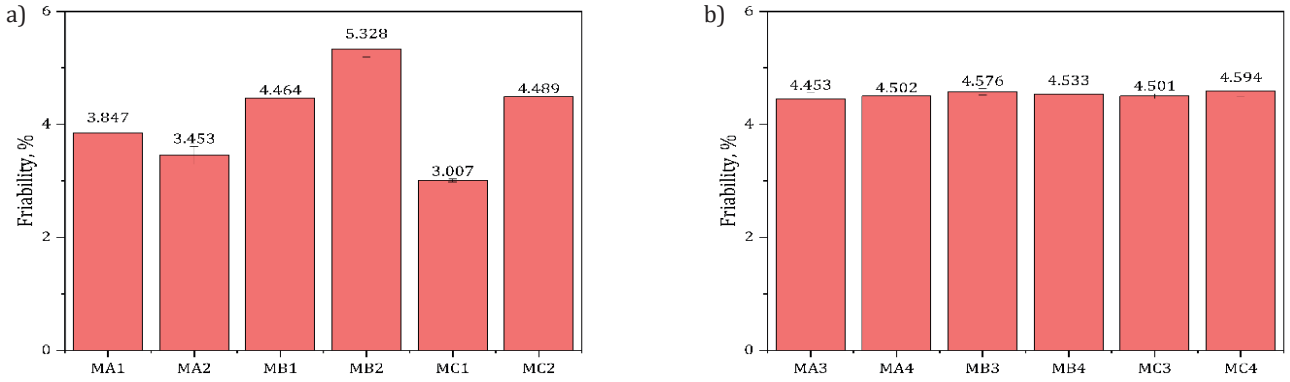

Fig. 8. The influence of binder type on friability of tested moulding sands: a) thermal hardening in a dryer; b) thermal hardening by microwaves

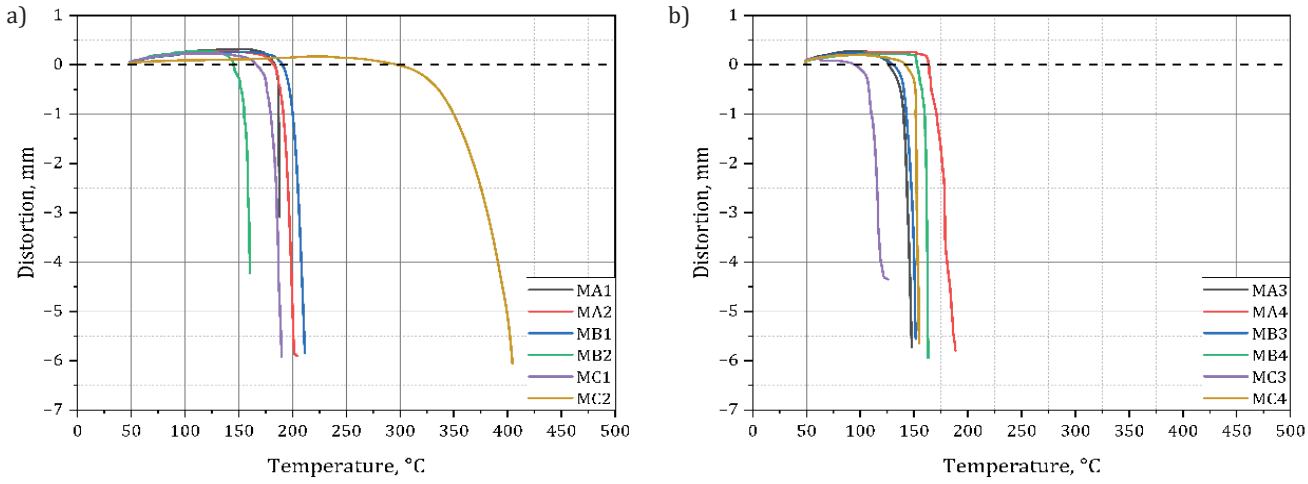

Fig. 9. The influence of binder type on hot distortion parameter in function of temperature: a) thermal hardening in a dryer; b) thermal hardening by microwaves

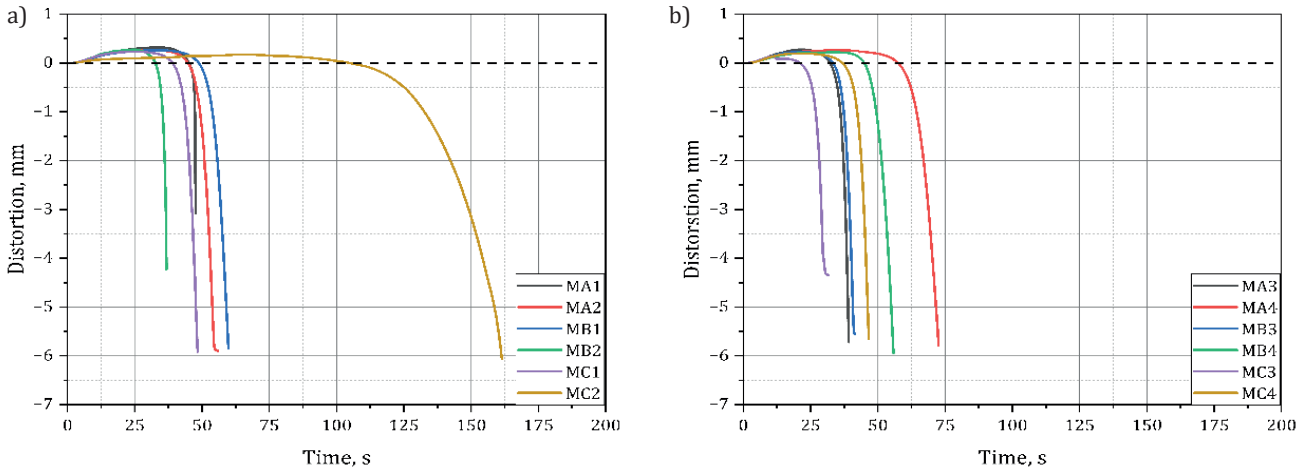

Fig. 10. The influence of binder type on hot distortion parameter in function of time: a) thermal hardening in a dryer; b) thermal hardening by microwaves

Analysis of the test results showed that all the moulding compounds tested exhibit thermal deformation typical for compounds with inorganic binders (Figs. 9 and 10). Most of the mixtures show thermal resistance for up to approximately 50 s. The exception is the MC2 mixture, which is thermally resistant for up to 161.2 s and at temperatures up to 404.9°C. The lowest thermal stability is characteristic of the MB2 mixture – the standard test specimen deformed after 36.8 s at a temperature of 124.6°C. In the case of microwave-cured compounds, the lowest thermal resistance is characteristic of the MC3 compound – the standard test specimen deformed after 31.8 s of heating at a temperature of 134.3°C. The best thermal stability is exhibited by the sand with sodium silicate binder A – MA3 – the standard test specimen deformed after 72.6 s of heating at a temperature of 188.4°C.

3. CONCLUSIONS

Based on the conducted research, the following conclusions can be drawn:

- New, modified inorganic binders developed for 3D printing of moulds and cores using Binder Jetting technology can be used as binding materials in thermally cured moulding sands.
- It is possible to use thermal curing carried out both in a dryer and in a microwave oven for the production of moulds and cores using inorganic binders developed for use in 3D printing technology (binder jetting).
- The best parameters for curing in a dryer were obtained for compounds containing 2.0 p.p.w. of binder cured at 160°C for 10 min.
- The best parameters for microwave curing in an 800 W microwave oven at a frequency of 2.45 GHz were obtained for compounds containing 2.0 p.p.w. during 6 minof curing.
- The chosen technological properties of moulding compounds with binders developed on the basis of commercial binders for use in 3D printing technology, thermally cured in a dryer, do not differ significantly from the properties of compounds with commercial binders. However, a decrease in the strength of microwave-cured mixtures with new binders was observed in comparison to mixtures with classic binders.
- The method of thermal curing and the modification of binders do not adversely affect the thermal stability of the tested compounds.
- The most important part of these results significantly shows that used materials and techniques have huge potential for use as inorganic binders in 3D printing Binder Jetting technology.
- In the next phase of the research, the feasibility of using new binding systems in semi-industrial and industrial settings will be evaluated, including their potential application in the production of casting molds and cores using the Binder Jetting method.

ACKNOWLEDGEMENT

Authors thank Chemical Plant "RUDNIKI" and SAND TEAM, spol. s r.o. for supplying some materials for the experiments.

The research was cofinanced within the NetCastPL4.0 project. The project is funded by the European Union under the Horizon Europe Programme, Grant Agreement No. 101159771.

The research was cofinanced by AGH Research Project No. 501.00 170000 10000 (16.16.170.654/B02) and National Science Centre (NCN) Grant No. 2021/41/B/ST5/02632.

REFERENCES

[1] Major-Gabryś K. (2016). *Environmentally Friendly Foundry Molding and Core Sand. Odlewnicze masy formierskie i rdzeniowe przyjazne dla środowiska.* Katowice – Gliwice: Wydawnictwo Archives of Foundry Engineering.

[2] Jelinek P. (2005). Rozwój spoiw nieorganicznych do dehydratacyjnego utwardzania mikrofalowego. In: *VIII Konferencja Odlewnicza Technical 2005*. Nowa Sól, pp. 5–11.

[3] Puzio S. (2022). *Dobór rodzaju oraz technologii utwardzania mas formierskich przeznaczonych na formy do ablacyjnego odlewania stopów aluminium* [PhD thesis]. Kraków: Akademia Górniczo-Hutnicza.

[4] Stachowicz M., Granat K. & Nowak D. (2010). Effect of hardening method and structure of linking Bridges on strengh of water glass moulding sands. *Archives of Foundry Engineering*, 10(Spec. Issue 2), 141–146.

[5] Stachowicz M., Granat K. & Pałyga Ł. (2016). Effect of sand wetting on physically hardened moulding sands containing a selected inorganic binder. Part 1. *Archives of Foundry Engineering*, 16(1), 73–78. DOI: https://doi.org/10.1515/afe-2016-0006.

[6] Kaczmarska K., Grabowska B., Drożyński D., Kurleto Ż. & Szymański Ł. (2015). An assessment of the effectiveness a physical curing methods of moulding sand bonded by binder based on starch and aluminosilicates. *Metallurgy and Foundry Engineering*, 41(3), 133. DOI: https://doi.org/10.7494/mafe.2015.41.3.133.

[7] Stachowicz M., Granat K. & Nowak D. (2011). Application of microwaves for innovative hardening of environment-friendly water-glass moulding sands used in manufacture of cast-steel castings. *Archives of Civil and Mechanical Engineering*, 11(1), 209–219. DOI: https://doi.org/10.1016/S1644-9665(12)60184-8.

[8] Stachowicz M., Granat K. & Pałyga Ł. (2016). Effect of sand wetting on physically hardened moulding sands containing a selected inorganic binder. Part 2. *Archives of Foundry Engineering*, 16(1), 79–84. DOI: https://doi.org/10.1515/afe-2016-0007.

[9] Grabowska B. (2019). *Polimery. Budowa, otrzymywanie, właściwości, aplikacje w odlewnictwie*. Kraków: AKAPIT.

[10] Liu J., Shi X., Zhang G. & Li L. (2023). Study the mechanical properties of geopolymer under different curing conditions. *Minerals*, 13(5), 690. DOI: https://doi.org/10.3390/min13050690.

[11] Garcia-Lodeiro I., Palomo A., Fernández-Jiménez A. & Macphee D.E. (2011). Compatibility studies between N-A-S-H and C-A-S-H gels. Study in the ternary diagram Na_2O–CaO–Al_2O_3–SiO_2–H_2O. *Cement and Concrete Research*, 41(9), 923–931. DOI: https://doi.org/10.1016/j.cemconres.2011.05.006.

[12] Major-Gabryś K. A. & Halejcio D. M. (2025). Selection of Chemically Cured Molding Sands' with Inorganic Binders Dedicated to 3D Sand Printing. *Archives of Foundry Engineering*, 25(4), 81–90. DOI: https://doi.org/10.24425/afe.2025.155383.

[13] Halejcio D.M. & Major-Gabryś K.A. (2024). The comparison of chosen – bonded with the use of classical and dedicated for 3D printing furfuryl binder – molding sands' properties as a basis for development a new inorganic system. *Archives of Foundry Engineering*, 4, 49–55. DOI: https://doi.org/10.24425/afe.2024.151309.

[14] Halejcio D. & Major-Gabryś K. (2024). Dobór parametrów utwardzania spoiw nieorganicznych przeznaczonych do druku 3D mas formierskich. In: *Materiały konferencyjne: Szkoła Inżynierii Materiałowej SIM 2024*, Kraków: Akademia Górniczo-Hutnicza, p. 20. URL: https://sim.agh.edu.pl/home/sim/Grafiki/SIM2024_-_Materialy_Konferencyjne.pdf.

[15] Chavez L.A., Ibave P., Wilburn B., Alexander D., Stewart C., Wicker R. & Lin Y. (2020). The influence of printing parameters, post-processing, and testing conditions on the properties of binder jetting additive manufactured functional ceramics. *Ceramics*, 3(1), 65–77. DOI: https://doi.org/10.3390/ceramics3010008.

[16] Castro-Sastre M.Á., Fernández-Abia A.I., Piep J., Rodríguez-González P. & Barreiro J. (2020). Towards functional parts by binder jetting calcium-sulphate with thermal treatment post-processing. *Materials*, 13(17), 3818. DOI: https://doi.org/10.3390/ma13173818.

[17] Colton T. & Crane N.B. (2021). Influence of droplet velocity, spacing, and inter-arrival time on line formation and saturation in binder jet additive manufacturing. *Additive Manufacturing*, 37, 101711. DOI: https://doi.org/10.1016/j.addma.2020.101711.

[18] Cheny T., Colin C. & Verquin B. (2024). Experimental evaluation of binder infiltration depth and axial overlap to control properties of green parts produced by Binder Jetting. *Additive Manufacturing*, 87, 104231. DOI: https://doi.org/10.1016/j.addma.2024.104231.

[19] Bertolini F., Mariani M., Mercadelli E., Baldisserri C., Galassi C., Capiani C., Ardito R. & Lecis N. (2024). 3D printing of potassium sodium niobate by binder jetting: Printing parameters optimisation and correlation to final porosity. *Journal of Materials Research and Technology*, 29, 4597–4606. DOI: https://doi.org/10.1016/j.jmrt.2024.02.145.

[20] Diener S., Schubert H., Held A., Katsikis N., Günster J. & Zocca A. (2022). Influence of the dispersant on the parts quality in slurry-based binder jetting of SiC ceramics. *Journal of the American Ceramic Society*, 105(12), 7072–7086. DOI: https://doi.org/10.1111/jace.18693.

[21] Chemical Plant "RUDNIKI" (n.d.). Sodium Water Glass. URL: https://zchrudniki.com.pl/oferta/szklo-wodne-sodowe [7.02.2026].

[22] Chemical Plant "RUDNIKI" (n.d.). Casting binders. URL: https://zchrudniki.com.pl/oferta/spoiwa-odlewnicze [7.02.2026].

[23] SAND TEAM spol. s r. o. (n.d.). GEOPOL®. URL: https://www.sandteam.cz/pl/produkcja-spoiw/ [7.02.2026].

[24] Lewandowski J.L. (1986). *Materiały formierskie. Laboratorium, Skrypty Uczelniane nr 1008 Akademii Górniczo-Hutniczej im. S. Staszica w Krakowie*. Kraków: Wydawnictwo Akademii Górniczo-Hutniczej im. St. Staszica w Krakowie.

[25] Anwar N., Major-Gabryś K., Jalava K. & Orkas J. (2024). Effect of additives on heat hardened inorganic solid foundry binder. *International Journal of Metalcasting*, 19(1), 129–144. DOI: https://doi.org/10.1007/s40962-024-01277-w.

[26] Jakubski J. & Dobosz S.M. (2006). Wpływ powłoki ochronnej na zjawiska cieplne w rdzeniach odlewniczych. *Archives of Foundry Engineering*, 6(18), 453–458.

Journal of Casting & Materials Engineering Vol. 10 No. 1 (2026) 10–15
https://doi.org/10.7494/jcme.2026.10.1.10-15

Determination of the Heat Transfer Coefficient in the Isothermal Quenching Process of ADI Cast Iron Cooled with Water Mist

Andriy Burbelko[a], Piotr Stręk[a*]

[a] AGH University of Krakow, Faculty of Foundry Engineering, 23 Reymonta St., 30-059 Krakow, Poland
**e-mail: piotr@ledavi.com*

Received: 12 March 2026/Accepted: 19 March 2026/Published online: 31 March 2026.
This article is published with open access at AGH University of Science and Technology Journals.

Abstract

Isothermal quenching of austempering cast iron (ADI) castings requires that, after austenitization the casting must be rapidly cooled to the temperature of isothermal austenite decomposition. The cooling rate throughout the entire volume of the heat-treated product must be high enough to prevent pearlitic transformation. At the same time, the temperature of the cooled surface must not decrease below the martensitic transformation start temperature M_s. The cooling rate of the casting surface is determined by factors such as the temperature difference between the surface of the cooled casting and the cooling medium, the thermal conductivity of cast iron, the heat transfer coefficient, and the wall thickness of the treated casting. In the case of cooling with water mist, the heat transfer coefficient depends on the temperature of the cooled surface. To control the cooling process of castings using water mist, information about this relationship for the temperature range of 200–800°C is needed. Available scientific publications on this subject contain contradictory data.

Therefore, a measuring station was built with the ability to set the temperature of the cooled surface. The station includes a measuring system that allows the measurement of the heat flux flowing from the heating element into the environment. The result of the research is the measurement of the relationship between the temperature of the cooled surface and the heat transfer coefficient. The values obtained will be used in the future to build a numerical model of ADI castings heat treatment. This work may contribute to the future replacement of salt baths (currently used for fast cooling and austempering) with water mist spraying. In this case, the low-temperature operation of austenite decomposition can be performed without the use of salt a bath.

Keywords:

austempered ductile iron, austempering, water mist, heat transfer coefficient, heat treatment

1. INTRODUCTION

Article [1] presents the theoretical possibilities of controlling the cooling rate in the heat treatment of cast iron using water mist spraying. The advantages of using water mist include: economics, the high specific heat of the phase transition of water droplet evaporation, and environmental friendliness. These advantages have been recognized by numerous researchers, including [2] and [3]. However, one challenge when applying this method is achieving precise control of heat transfer to prevent the M_s temperature from reaching the surface layer of the cooled casting. There are many publications on the measurement of the heat transfer coefficient during the spray cooling of metal surfaces with water mist. In these studies the coefficient was determined using the conduction equation under either steady state [4–7] or unsteady state [8–16] heat flow conditions.

Unfortunately, the research methods and results presented in the literature do not cover the temperature range of interest to us, including ADI isothermal hardening and a material such as cast iron. Therefore, a research method has been designed and presented in this article to fill the research gap not yet represented in the literature. It should be noted that many factors influence the value of the determined coefficient. These factors include the size of the spray droplets and their velocity and the water flow rate. The influence of these parameters, among others, have been investigated and described in publication [17]. The effects of the type of cooled material and the roughness of the cooled surface are described in [18, 19]. At this stage of the research the above factors were assumed to be constant. The examined dependence of the heat transfer coefficient on temperature will be used to create a numerical model that would describe the phenomena occurring during the cooling of austempered ductile iron. The proposed measurement method is based on established heat transfer conditions.

2. TEST SETUP

The measurement system is shown schematically in Figure 1. The plate (2) made of ductile iron is cooled on one side by water spray (3) and heated on the other side (4). A type K thermocouple (1) is welded to the heated side of the plate. A diagram of the plate and the location of the thermocouple weld is shown in Figure 2. The cooled surface of the plate has not been machined and corresponds to the surface of the casting after it has been removed from the mold. The temperature is measured by a Keysight 34465A multimeter (7), while the measurement is set by a trigger controller (8). The individual parts of the heating element are designed in such a way that heat is released in the part located directly under the measuring plate (Figs. 3 and 4). This reduces heat loss. In addition, a layer of thermally conductive adhesive is used thatimproves heat transfer between the heating element and the test plate. The heating element is insulated with ceramic tiles to limit heat transfer to the environment other than through the measuring plate. The heating element is connected via a discrete transistor current controller (6) to a power supply with a capacity of 300 A and a voltage of 5 V. The connecting cables for the high-current part have a cross-section of 2×35 mm^2. The discrete current and power output controller on the heating element is implemented using parallel-connected MOSFET transistors controlled by integrated gate controllers. The discrete current controller (6) is galvanically isolated from the trigger controller (8) by a fiberoptic link. The Keysight DAQ970A data logger (9) and the appropriate card attached to the logger (Keysight DAQM901A) are used to measure the current and voltage on the heating element. The voltage is measured directly by the data logger, while the current is measured by the LT1000-TI current-voltage converter (5). The voltage generated by the converter is proportional to the current flow in the high-voltage cables supplying the heating element. Measurements taken by the multimeter and recorder are read cyclically using a PC (10). The data is read via an Ethernet connection and processed by proprietary software. The cyclical temperature reading is used by a software-implemented PI (proportional integral) controller to determine the deviation between the set temperature and the temperature read from the thermocouple. The calculated deviation is the basis for calculating the duty cycle of the control pulse that opens the MOSFET transistors in the current controller (6). Data on the desired duty cycle is sent from the computer in digital form to the trigger controller (8).

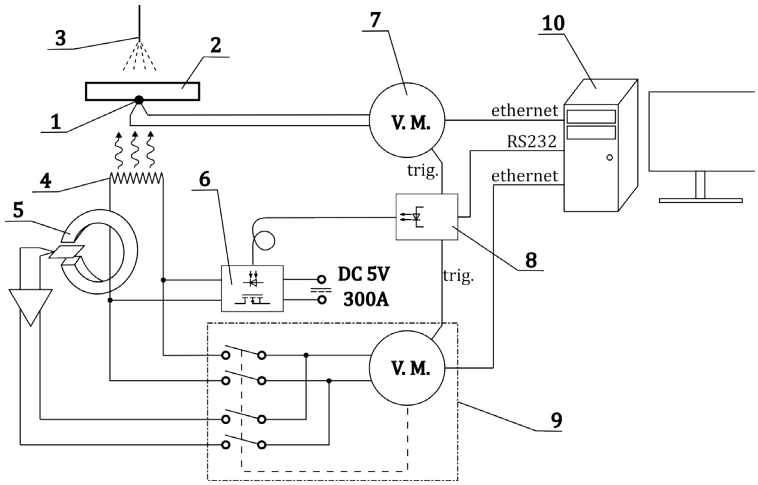

Fig. 1. Measurement system diagram: 1 – thermocouple, 2 – measuring plate, 3 – spray nozzle, 4 – heating element, 5 – current voltage converter, 6 – discrete current controller, 7 – multimeter, 8 – measurement trigger controller, 9 – data logger, 10 – PC

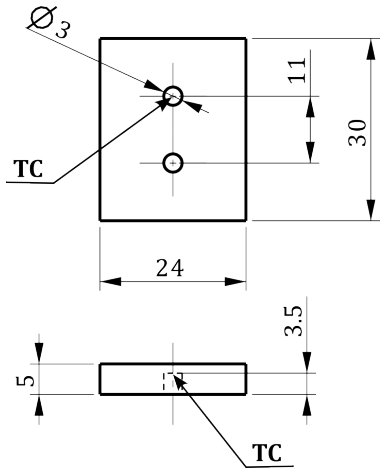

Fig. 2. Dimensions of the measuring plate (TC – thermocouple welding point)

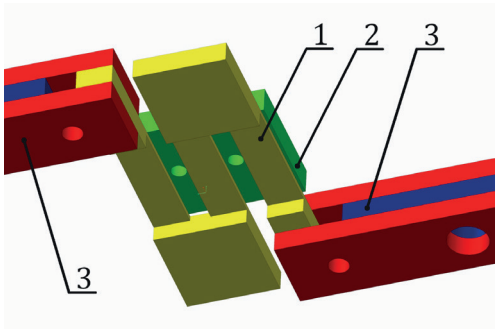

Fig. 3. Mutual position of the test plate and the heating element: 1 – heating element, 2 – measuring plate, 3 – power supply terminals

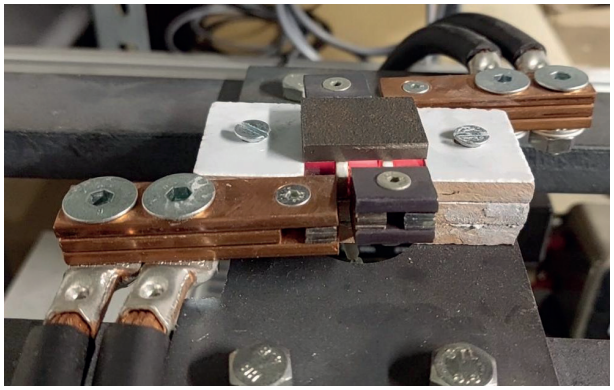

Fig. 4. Heating element with ceramic insulation and measuring plate

The hydraulic-air system diagram is shown in Figure 5. The heated measuring plate is cooled using a single-phase full-cone nozzle with a spray angle of 30° (3); manufacturer's symbol: BEX 1/8GS3001.4 V2A. The hydraulic-air system cycle begins with filling the water tank (1) by opening the valve supplying water from the water supply network. The filling is checked by observing the overflow valve. The valve supplying compressed air remains closed at this point. After filling the tank the water supply and overflow valves are closed. In the next step the compressed air tank (2) is filled to a pressure of 8 bar using a compressor (5). Once this pressure is reached the safety switch opens the compressor's power supply. The desired water outlet pressure is set on the pressure reducer (4). To start the measurement the valve supplying air to the water tank is opened, followed by the valve connecting the spray nozzle (3) and the water tank (1).

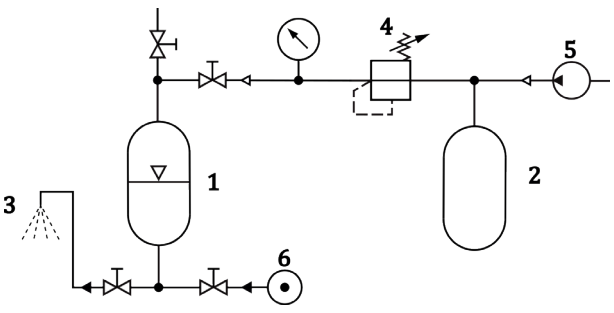

Fig. 5. Diagram of the hydraulic-air system of a heat transfer coefficient measurement station: 1 – cooling water tank, 2 – compressed air tank, 3 – spray nozzle, 4 – pressure reducer, 5 – compressor, 6 – service water supply

Figure 6 shows a heated measuring plate made of cast iron cooled by active water-mist spraying. A trough is visible, the task of which is to collect and feed unused water to cool the measuring plate and protect components that not get wet.

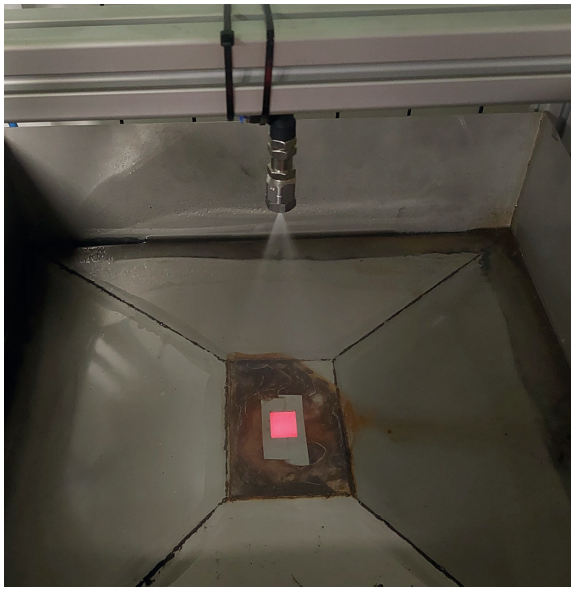

Fig. 6. View of the station during the research

3. MEASUREMENT CONDITIONS AND RESULTS

In the first step the nozzle capacity was tested. It amounted to 0.55 l/min at a pressure of 3 bar. The distance between the nozzle and the measuring plate is 200 mm. Considering that the spray angle of the nozzle is 30°, the surface area sprayed by the nozzle is $9.022 \cdot 10^{-3}$ m^2, while the surface area of the measuring plate onto which the spray falls is 0.024 m × 0.030 m = $0.72 \cdot 10^{-3}$ m^2. A test was carried out that showed that the sprayed stream has the same efficiency over the entire sprayed surface (Fig. 7). The test consisted of measuring the height L of the water column in a measuring cup during 1 minute of nozzle operation. The test was carried out at 6 points on the sprayed surface. No deviations in height L were found during the measurement.

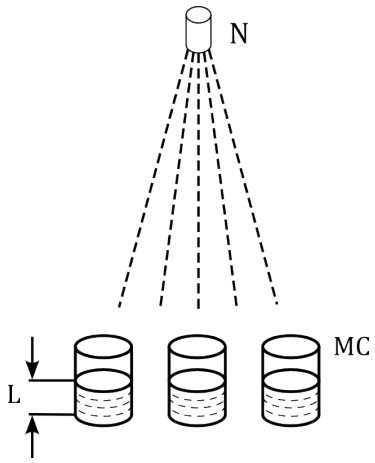

Fig. 7. Schematic representation of spray-intensity uniformity measurement, where N – nozzle, MC – measuring cup

Therefore, the η_m spray consumption converted to the sprayed tile surface area could be calculated using the following formula:

$$\eta_m = \rho_v \cdot \left(\frac{P_p}{P_c} \right) \quad (1)$$

where:

η_m – spray rate converted to the sprayed surface area of the measuring plate, g/s,
ρ_v – nozzle capacity (9.166 g/s),
P_c – total area sprayed by the nozzle ($9.02 \cdot 10^{-3}$ m^2),
P_p – the surface area of the tile that was sprayed ($0.72 \cdot 10^{-3}$ m^2),

The spray coefficient, converted to the sprayed surface area of the test panel, is: $\eta_m = 0.731$ g/s

We assumed that all of the water sprayed onto the tile surface would be heated to 100°C and then converted into steam. In our calculations we ignored the specific heat of the water vapor. The total maximum power that could be dissipated from the sprayed tile surface under these assumptions could be calculated using the following formula:

$$P_c = \left[c_V \cdot (100 - 20) + c_p \right] \cdot \eta_m \quad (2)$$

where:

P_c – theoretical total power that could be dissipated by water mist spray,
c_V – the specific heat of the water (4.184 kJ/(kg·K)),
c_p – the heat of the vaporization of the water (2260 kJ/kg).

After substituting the data we obtained the maximum power that could be dissipated from the surface of the plate at a level of P_c = 1895.9 W, which gave a theoretical heat flux intensity of 2633 kW/m^2.

In the second step, thanks to the PI controller, the target temperature value T_m, measured by the thermocouple was set (Fig. 8), which, under the designed geometric conditions (Fig. 2), was very close to T_p. After the measured temperature stabilized, ten measurements of the heat output Q_T were recorded. All measurement results are presented in Figure 9.

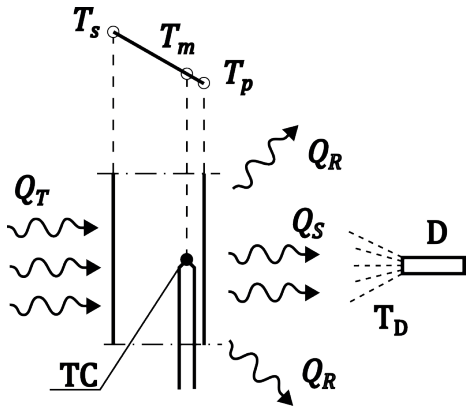

Fig. 8. Temperature field and thermocouple (TC) location: T_s – heating element temperature, T_m – thermocouple temperature, T_p – surface temperature, T_D – water mist temperature, Q_T – heat emitted by the heating element, Q_R – heat flux flowing to the environment in a manner other than through the cooled surface of the test plate, Q_S – heat flux dissipated by water mist spray

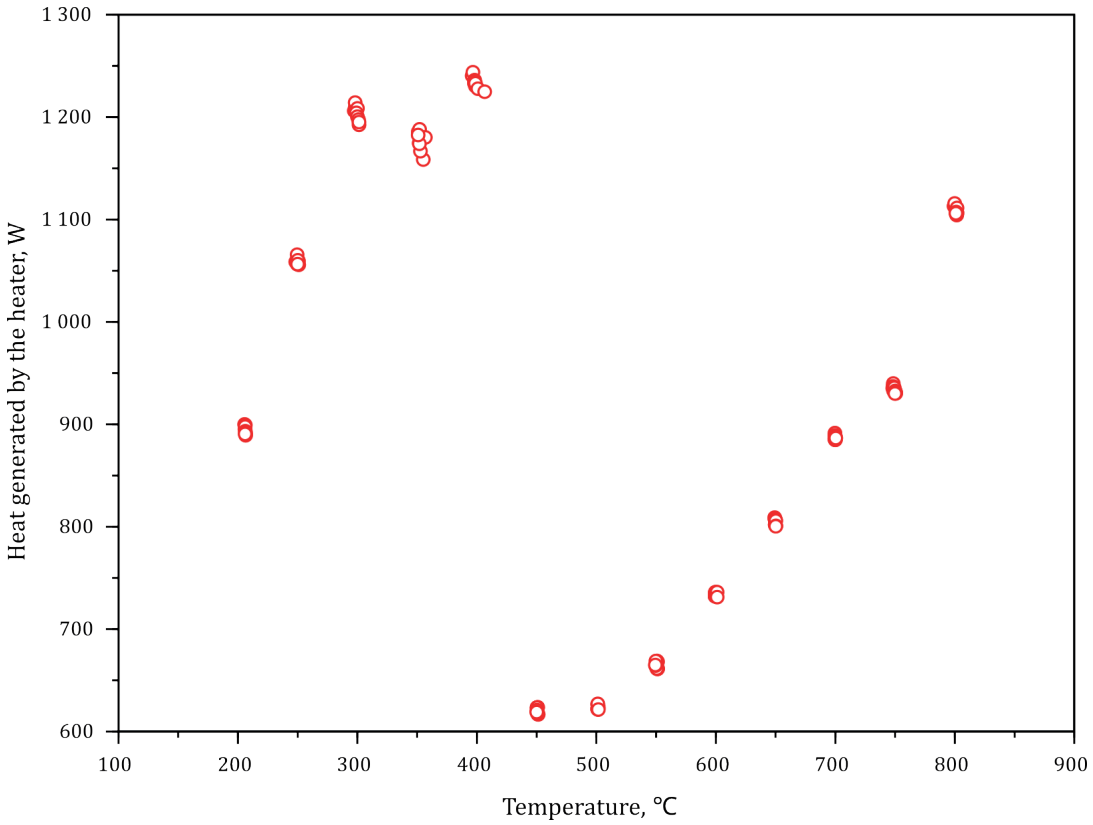

Fig. 9. Power dissipated on the heating element as a function of temperature

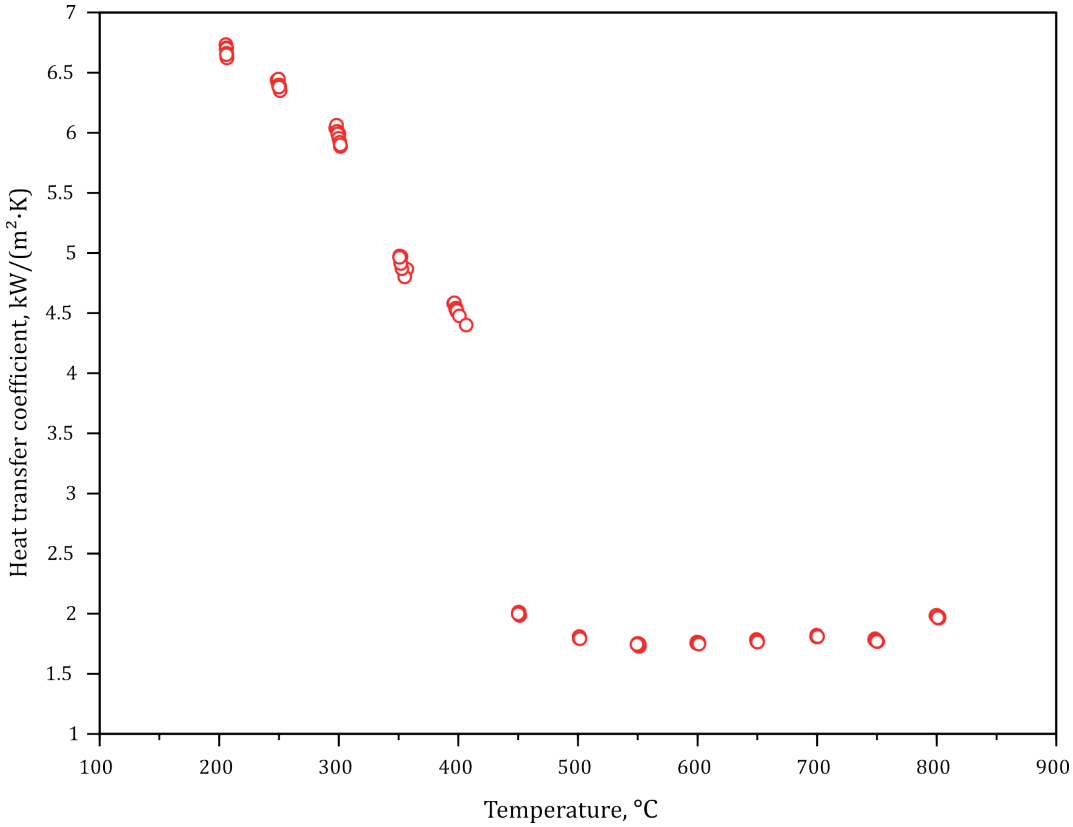

Fig. 10. Heat transfer coefficient as a function of temperature

Using the quantitative data from the power dissipated on the heating element, the heat transfer coefficient was calculated as a function of surface temperature from the equation (in connection with Figure 8):

$$\alpha = \left(\frac{Q_T}{T_D - T_m} \right) \tag{3}$$

The results of the calculations are presented in Figure 10. The results obtained are consistent with those obtained by other researchers [5]. The advantage of the presented research is that it provides results for the entire temperature range occurring in the isothermal quenching process for obtaining an ausferrite structure in ductile iron. The sharp observed change in heat generation (Fig. 9) and in the heat transfer coefficient (Fig. 10) within the 400–450°C temperature range is associated with the well-known effect of vapor-jacket formation effect. This layer prevents direct contact between the evaporating liquid and the metal surface. The described effect and the temperature at which this transition occurs were named after Leidenfrost, the author who described the phenomenon [20].

4. DISCUSSION OF RESULTS

The advantage of the proposed test method is that it provides results across the entire range of temperatures of isothermal quenching of ADI. The Leidenfrost temperature was determined, which for the analyzed parameters of water mist and the test sample was in the range of 400–450°C. The results obtained are consistent with those published in [5]. This study is not without its flaws. Namely, it is difficult to estimate or measure heat losses, i.e., the heat flux Q_R flowing from the heating element to the environment by means other than through the test plate (Fig. 8). In the study the heat transfer coefficient was assessed on the basis of the power emitted by the heating element under conditions of stable recorded sample temperature. Under these conditions, most of the heat dissipated was related to the heating and evaporation of the sprayed water droplets. However, there were heat losses associated with the cooling of other components of the installation that were not exposed to the spray. These losses caused the results to be overestimated in relation to the actual value but do not affect the assessment of the Leidenfrost temperature. At this stage, the value of these losses in relation to the heat output was not quantitatively assessed.

5. SUMMARY

1. The results of the study indicate the potential for using water mist as a cooling medium in the processing of ADI cast iron as an alternative to molten salts.
2. The study showed that the heat transfer coefficient via spraying (1700–6700 W/(m²·K)) is significantly higher than that for a salt bath (550–1100 W/(m²·K)) [21], which is significant because, with proper control, a cooling profile can be achieved that is unattainable with conventional heat treatment using other cooling media.
3. The results of the study, covering such a wide measurement range provide a basis for developing a more comprehensive numerical model of heat treatment of ADI cast iron using water mist.

REFERENCES

[1] Stręk P. (2024). Theoretical possibilities of controlling the cooling rate in the heat treatment of cast iron with water mist. *Journal of Casting & Materials Engineering*, 8(4), 68–73. DOI: https://doi.org/10.7494/jcme.2024.8.4.68.

[2] Władysiak R., Kozuń A. & Pacyniak T. (2017). The effect of water mist cooling of casting die on the solidification, microstructure, and properties of AlSi20 alloy. *Archives of Metallurgy and Materials*, 62(1), 187–194. DOI: https://doi.org/10.1515/amm-2017-0026.

[3] Czekaj E., Kwak Z. & Garbacz-Klempka A. (2017). Comparison of impact of immersed and micro-jet cooling during quenching on microstructure and mechanical properties of hypoeutectic silumin AlSi7Mg0.3. *Metallurgy and Foundry Engineering*, 43(2), 153–168. DOI: https://doi.org/10.7494/mafe.2017.43.3.153.

[4] Mudawar I. & Valentine W.S. (1989). Determination of the local quench curve for spray-cooled metallic surfaces. *Journal of Heat Treating*, 7(2), 107–121. DOI: https://doi.org/10.1007/BF02833195.

[5] Flores T., Castillejos H. & Thomas B. (2017). Heat extraction and droplet impact regimes obtained with continuous casting air-mist nozzles. *AISTech 2017 Proceedings of the Iron & Steel Technology Conference. Vol. II*, Nashville, TN, USA, pp. 1751–1760.

[6] Tenzer F.M. (2020). *Heat transfer during transient spray cooling: An experimental and analytical study* [PhD thesis]. Fachbereich Maschinenbau der Technischen Universität Darmstadt, Darmstadt.

[7] Puschmann F., Schmidt J. & Specht E. (2000). Evaporation quenching with atomized sprays. *Proceedings of the 3rd European Thermal Science Conference*, Heidelberg, pp. 1071–1074.

[8] Sözbir N., Chang Y. & Yao S. (2003). Heat transfer of impacting water mist on high temperature metal surfaces. *Journal of Heat Transfer*, 125(1), 70–74. DOI: https://doi.org/10.1115/1.1527913.

[9] Jasiewicz E., Hadała B., Cebo-Rudnicka A., Malinowski Z. & Jasiewicz K. (2023). Comparison of the heat transfer efficiency of selected water cooling sytems. *SSRN Electronic Journal*. DOI: https://doi.org/10.2139/ssrn.4333923.

[10] Fang Y. Sabariman S. Specht E. (2016). Analytical Model for Describing Experimental Results on Parameters Influencing Heat transfer in Film Boiling with Spray Quenching. *Proceedings of 12th International Conference on Heat Transfer, Fluid Mechanics and Thermodynamics, Costa del Sol, Malaga, Spain.*

[11] Labergue A., Lemoine F., Aiguier T. & Gradeck M. (2014). Comparative study of the cooling of a hot temperature surface using spray and liquid jet. In: *15th International Heat Transfer Conference (IHTC-15), 2014. Kyoto, Japan*, pp. 2415–2429. DOI: https://doi.org/10.1615/IHTC15.evp.009287.

[12] Pohanka M. & Kotrbáček P. (2012). Design of Cooling Units for Heat Treatment. In: Czerwinski F. (Ed.), *Heat Treatment – Conventional and Novel Application.* DOI: https://doi.org/10.5772/50492.

[13] Van der Geld C.W.M., Passos J.C. & Leocadio H. (2019). Heat transfer coefficient during water jet cooling of high-temperature steel. In: *11th International Rolling Conference, (IRC 2019) São Paulo*, pp. 763–773. DOI: https://doi.org/10.5151/9785-9785-32400.

[14] Hadała B., Cebo-Rudnicka A. & Radziszewska A. (2022). Identification of the boundary condition of heat transfer during spray cooling process of the oxidized surface. *SSRN Electronic Journal*. DOI: https://doi.org/10.2139/ssrn.4167471.

[15] Fujimoto H., Hatta N., Asakawa H. & Hashimoto T. (1997). Predictable modeling of heat transfer coefficient between spraying water and a hot surface above the Leidenfrost temperature. *ISIJ International*, 37(5), 492–497. DOI: https://doi.org/10.2355/isijinternational.37.492.

[16] Cebo-Rudnicka A. (2011). *Wpływ warunków chłodzenia oraz przewodności cieplnej wybranych metali na współczynnik wymiany ciepła w procesie chłodzenia z natryskiem wodnym* [PhD thesis]. Kraków: Akademia Górniczo-Hutnicza.

[17] Władysiak R. & Budzyński P. (2012). Structure of water mist stream and its impact on cooling efficiency of casting die. *Archives of Foundry Engineering*, 12(2), 251–260. DOI: https://doi.org/10.2478/v10266-012-0069-y.

[18] Chabičovský M., & Horský J. (2017). Factors influencing spray cooling of hot steel surfaces. In: *Metal 2017, Brno, Czech Republic*. Brno: Brno University of Technology, Faculty of Mechanical Engineering, pp. 77–82. URL: https://www.confer.cz/metal/2017/read/1345-factors-influencing-spray-cooling-of-hot-steel-surfaces.pdf.

[19] Baumeister K.J., Henry R.E. & Simon F.F. (1970). Role of the surface in the measurement of the Leidenfrost temperature. In: Bergles A.E. & Webb R.L. (Eds.), *Augmentation of Convective Heat and Mass Transfer. Papers presented at the Winter Annual Meeting of the American Society of Mechanical Engineers*, New York: American Society of Mechanical Engineers. Heat Transfer Division, pp. 91–101.

[20] Leidenfrost J.G. (1966). On the fixation of water in diverse fire. *International Journal of Heat and Mass Transfer*, 9(11), 1153–1166. DOI: https://doi.org/10.1016/0017-9310(66)90111-6.

[21] Myszka D. & Babul T. (2006). Obróbka cieplna żeliwa sferoidalnego w złożach fluidalnych. *Archiwum Odlewnictwa*, 6(20), 177–184.

Journal of Casting & Materials Engineering Vol. 10 No. 1 (2026) 16–29
https://doi.org/10.7494/jcme.2026.10.1.16

Quaternionic Quantum Mechanics: the Particles, Their *q*-Potentials and Mathematical Electron Model

Bogusław Bożek[a], Marek Danielewski[b*], Lucjan Sapa[a]

[a] AGH University of Krakow, Faculty of Applied Mathematics, 30 Mickiewicza Av., 30-059 Krakow, Poland
[b] AGH University of Krakow, Faculty of Materials Science and Ceramics, 30 Mickiewicza Av., 30-059 Krakow, Poland
**e-mail: daniel@agh.edu.pl*

Received: 8 August 2025/Accepted: 15 December 2025/Published online: 31 March 2026.
This article is published with open access at AGH University of Science and Technology Journals.

Abstract

In this work we show the quaternionic quantum descriptions of physical processes from the Planck to macro scale. The results presented here are based on the concepts of the Cauchy continuum and the elementary cell at the Planck scale. The structurally symmetric quaternion relations and the postulate of the quaternion velocity have been important in the present development. The momentum of the expansion and compression $\dot{u}_0(t, x)$ is the consequence of the scalar term $\sigma_0(t, x)$ in the quaternionic deformation potential. The quaternionic $G_0(m)(\sigma_0 + \hat{\phi})$, vectorial $G_0(m)\hat{\phi}$ and scalar $G_0(m)\sigma_0$ propagators are used to generate the second order PDE systems for the proton, electron and neutron. A mathematical model of an electron is formulated. It is described by the hyperbolic-elliptic partial differential system of quaternion equations with the initial-boundary conditions. The boundary conditions are generated by the quaternion energy flux that is found with the use of the Gauss theorem, the Cauchy–Riemann derivative and other mathematical formulas. The rigorous assessment of the second order PDE systems allows the proposal of two second order PDE systems for the *u* and *d* quarks from the *up* and *down* groups. It was verified that both the proton and the neutron obey experimental findings and are formed by three quarks. The proton and neutron are formed by the *d*-*u*-*u* and *d*-*d*-*u* complexes, respectively. The *u* and *d* quarks do not comply with the Cauchy equation of motion. The inconsistencies of the quarks' PDE with the quaternion forms of the Cauchy equation of motion account for their short lifetime and the observed Quarks Chains. That is, they explain the Wilczek phenomenological paradox: *Quarks are Born Free, but everywhere they are in Chains*.

Keywords:

ideal elastic solid, electron, quaternionic potential, vectorial potential, proton, electron, quark chains

1. INTRODUCTION

After developing the Hilbert space formulation of quantum mechanics [1], von Neumann looked into higher mathematical analysis, i.e., rings of operators, in an attempt to get rid of some of the *ad hoc* postulates of quantum mechanics. In 1936, together with Birkhoff, he suggested the Quaternionic Quantum Mechanics (QQM), where wave functions or probability amplitudes are quaternion valued [2]. However, despite this early development, systematic work on the quaternionic extension of quantum mechanics has not yet begun. The essential results relevant to the present paper are by Lanczos. His dissertation was on a quaternionic field theory of the classical electrodynamics [3, 4]. In his derivation of the Dirac equation [5], there is a doubling in the number of solutions and the concepts that still remain at the front of the fundamental theory. These articles were unnoticed by contemporaries; Lanczos abandoned quaternions and never returned to Quaternionic Field Theory (QFT).

Almost immediately it was demonstrated that the Cauchy–Riemann type conditions in the quaternion representation are identical in the shape to vacuum equations of electrodynamics [6] and that the Dirac transition amplitudes are quaternion valued [7]. Christianto derived an original wave equation from the correspondence between the Dirac equation and the Maxwell electromagnetic equations via the biquaternionic representation [8]. The Adler schema of the quaternionizing the quantum mechanics inspired the Harari–Shupe's model for the composite quarks and leptons [9, 10] and the substantial progress in the QQM and QFT [11]. Adler presented a major conceptual advance for the purpose of determining whether a quaternionic Hilbert space is suitable for the unification of the standard model forces with gravitation. He provided an introduction to the problem of formulating quantum field theories and concluded that the QQM may fit into the physics of unification and measurement theory issues [12]. Arbab [13] found a quaternionic wave function consisting of real and scalar functions satisfying the quaternionic momentum eigenvalue equation. More recently in [14] he proposed a quaternionic commutator bracket. Giardino considered in [15] the generalization of the imaginary units within the instances of the complex quantum mechanics, and the quaternionic quantum mechanics. The real Hilbert space formalism

developed within the QQM was applied by Giardino in [16] to the simple model of the autonomous particle.

The focus here is on quaternion quantum mechanics and the quaternionic field theory. The QQM presented here is ontological in a sense that it starts with being, that are the Cauchy ideal elastic continuum at the macro-scale ($> 10^{-20}$ m) and the "Planck unit cell" at the micro-scale ($\sim 10^{-35}$ m) [17, 18]. The basic categories of being and their relations are governed by the quaternion algebra [18].

The evolution of the Planck–Kleinert Crystal (P-KC) model and the development of the QQM are shown in succeeding papers [18–21]. In this article we present the QQM in its most recent, refined form:

- We use the ontology-based formalism which is based on the Planck–Kleinert crystal concept [17] and the quaternion algebra introduced by Hamilton, Section 1.1.
- The widely used Helmholtz decomposition is employed in the general form in $\mathbb{R}^4$, Section 2.
- All vectors are in the $\mathbb{R}^4$ representation, e.g., the four-velocity is the "new" variable that allows for the symmetrization of the Hamiltonian [22] and the first and second order wave equations.
- Second order PDE systems of the quark particles are proposed.
- The mathematical model of an electron is formulated. It is described by the hyperbolic-elliptic partial differential system of quaternion equations with the initial-boundary conditions. This differential problem is decomposed onto the hyperbolic equation with the Neumann boundary condition on compression and the hyperbolic-elliptic subsystem on a twist with some specific boundary condition concerning rotation. The boundary conditions are generated by the quaternion energy flux that is found with the use of the Gauss theorem, the Cauchy–Riemann derivative and other mathematical formulas.
- Further studies are suggested in order to verify or refute those propositions.

The Cauchy model of the elastic continuum is presented in Section 1.2. We construct a Lagrangian with the use of the Cauchy–Riemann operator and introduce the key new concept, the quaternion valued velocity, in Section 2. Abbreviations used in the text are presented in the Appendix**.**

1.1. Quaternions

The elements of the quaternion algebra used in the QQM and QFT were already presented in [18–20]. The basic definitions and formulas of quaternions and quaternionic functions can be found in [23, 24].

In Hamilton's own words, he created the $\mathbb{R}^4$ analog of complex numbers as the equivalent of the time-space continuum [25]:

Time is said to have only one dimension, and space to have three dimensions. The mathematical quaternion partakes of both these elements; in technical language it may be said to be 'time plus space'... and in this sense it has, or at least involves a reference to, four dimensions.

We demonstrate here that Hamilton's *'time plus space'* is consistent with the Cauchy model of ideal elastic continuum in the quaternionic representation.

The algebra of quaternions $q = q_0 + \hat{q} \in \mathbb{H}$ has all properties of an algebra with the unity. The symbol $\hat{q}$ means a pure imaginary number.

The quaternionic deformation potential, i.e., the deformation four-potential or q-potential is a relativistic function from which the displacement field can be derived. It combines both a compression scalar potential q_0 and a torsion vector potential $\hat{q}$ (twist) into a single quaternion (four-vector) $q = q_0 + \hat{q} \in \mathbb{H}$.

The multiplication of quaternions is noncommutative: $p \cdot q \neq q \cdot p$. The noncommutativity of multiplication is the only property that makes quaternions different from real and complex numbers.

The quaternionic deformation potential is invariant in the sense of Lorentz.

An arbitrary quaternion $q \in \mathbb{H}$ can be written in the algebraic form:

$$q = q_0 + q_1 i + q_2 j + q_3 k, \tag{1}$$

where i, j, k are called imaginary units and fulfill the relations:

$$i^2 = j^2 = k^2 = -1, \quad ij = -ji = k, \quad jk = -kj = i, \quad ki = -ik = j. \tag{2}$$

It is also possible to represent quaternions by some matrices.

The commutator of two elements p and q is defined by the formula:

$$[p, q] = p \cdot q - q \cdot p = 2\hat{p} \times \hat{q} \tag{3}$$

and can be looked at as a measure of noncommutativity. Two quaternions commute, i.e., $[p, q] = 0$ if and only if their vector parts $\hat{p}$ and $\hat{q}$ are collinear.

Quaternion-valued functions describe a lot of useful physical models, e.g., the electric and magnetic fields [26], Section 3. Let $\Omega \subset \mathbb{R}^3$ be a bounded set. The so-called $\mathbb{H}$-valued functions have the form:

$$q(x) = q_0(x) + q_1(x)i + q_2(x)j + q_3(x)k, \quad x = (x_1, x_2, x_3) \in \Omega, \tag{4}$$

where the functions $q_0(x)$, $q_l(x)$, $l = 1, 2, 3$ are real-valued. Properties such as continuity, differentiability, integrability, and so on, have to be possessed by all the components $q_0(x)$, $q_l(x)$, $l = 1, 2, 3$. In this manner, the Banach, Hilbert, and Sobolev spaces of $\mathbb{H}$-valued functions can be defined [26]. In the Hilbert space over $\mathbb{H}$:

$$L^2(\Omega) = \{q : \Omega \to \mathbb{H} | \ \int_\Omega q_0^2 dx < \infty, \ \int_\Omega q_l^2 dx < \infty, \ l = 1, 2, 3\} \tag{5}$$

the inner product can be defined as follows:

$$\langle q_1, q_2 \rangle = \int_\Omega q_1^* \cdot q_2 dx, \quad q_1, q_2 \in L^2(\Omega). \tag{6}$$

The Fourier series, Lebesgue measure, Gelfand triples, Laplace transform, and many others on the vector space of $\mathbb{H}$-valued functions over $\mathbb{H}$ can be defined in a standard way as in the real and complex cases.

In the further part we use the Cauchy–Riemann operator D acting on the quaternion-valued functions $q(x) = q_0(x) + \hat{q}(x)$ of the form:

$$Dq = -\text{div}\, \hat{q} + \text{grad}\, q_0 + \text{rot}\, \hat{q}. \tag{7}$$

Similarly, the functions $q(t, x)$, depending on time t, may be considered.

Moreover, the exponential quaternionic function of quaternionic variables is very useful in applications and has the trigonometrical representation:

$$e^q = e^{q_0}\left(\cos|\hat{q}| + \frac{\hat{q}}{|\hat{q}|}\sin|\hat{q}|\right), \quad q = q_0 + \hat{q} \in \mathbb{H}. \tag{8}$$

Remark 1. *Hurwitz's theorem says that there are only four normed division algebras:* $\mathbb{R}$, $\mathbb{C}$, $\mathbb{H}$ *and the octonions algebra. Lagrange's four-square theorem in number theory states that every non-negative integer is the sum of four integer squares. This theorem may have applications in QQM.*

1.2. The Cauchy dispacement field: the theory ofelasticity and properties at the Planck scale

Cauchy finished the theory of the ideal elastic continuum in 1822 [27], while Poisson [28] immediately after studied the elementary waves. Neumann [29] gave the proof of uniqueness of the solutions of some initial-boundary value problems. The rigorous completeness proof was given by Duhem [30]. The Cauchy theory is the first real, well posed theory of elasticity using the continuum approach, where the macroscopic phenomena are described in terms of field variables [31]: the compression div $\boldsymbol{u}$, and the twist rot $\boldsymbol{u}$. The stress tensor of the ideal elastic continuum is given by

$$\boldsymbol{T} = \lambda\,\mathrm{tr}(\boldsymbol{D})\boldsymbol{I} + 2\mu\boldsymbol{D}, \tag{9}$$

where tr($\boldsymbol{D}$) is the trace of the strain tensor, **I** is the identity matrix and the two moduli of elasticity, λ and μ, are the material-dependent constants. It was shown by Cauchy and Saint Venant that if the particles composing a regular crystal interact pairwise through central forces, then there is an additional symmetry that implies the Poisson ratio 0.25 and equal Lamé's coefficients: $\lambda = \mu$ [32]. The identity grad div $\boldsymbol{u}$ = div grad $\boldsymbol{u}$ + rot rot $\boldsymbol{u}$ implies that the stress tensor becomes:

$$\begin{aligned}\mathrm{div}\,\boldsymbol{T} &= 2\mu\,\mathrm{grad\,div}\,\boldsymbol{u} + \mu\,\mathrm{div\,grad}\,\boldsymbol{u} = \\ &= 3\mu\,\mathrm{grad\,div}\,\boldsymbol{u} - \mu\,\mathrm{rot\,rot}\,\boldsymbol{u}.\end{aligned} \tag{10}$$

The Cauchy equation of motion generalizes: (1) the Newton laws of motion (the conservation of the linear and angular momenta) to an ideal elastic solid, and (2) the concept of stress in terms of the gradients in the displacement field $\boldsymbol{u}(t, x) \in \mathbb{R}^3$:

$$\rho\frac{\partial^2\boldsymbol{u}}{\partial t^2} = 3\mu\mathrm{grad\,div}\boldsymbol{u} - \mu\mathrm{rot\,rot}\boldsymbol{u} + \boldsymbol{F}, \tag{11}$$

where $\boldsymbol{F}$ is the force induced solely by the displacements caused by the entities already present in the elastic continuum. In the following sections we show that the force must be generalized and follows from the Cauchy–Riemann derivative of the deformation potential f caused by the particle waves, i.e., the force in $\mathbb{R}^4$ is the consequence of the 4-potential f produced by the particles.

From Equation (11) the vectorial representation of the energy density in the deformation field can be computed [31, 33]:

$$e = \frac{1}{2}\dot{\boldsymbol{u}}\circ\dot{\boldsymbol{u}} + \frac{3}{2}c^2(\mathrm{div}\boldsymbol{u})^2 + \frac{1}{2}c^2\mathrm{rot}\boldsymbol{u}\circ\mathrm{rot}\boldsymbol{u}, \tag{12}$$

where $\dot{\boldsymbol{u}} = \partial u/\partial t$. The symbol "$\circ$" means the standard inner product in $\mathbb{R}^3$.

In the following we consider the Cauchy continuum with a Face Centered Cubic (FCC) structure. The Young modulus Y describes tensile elasticity which is axial stiffness of the length of a body to deformation along the axis of the applied tensile force. It is related to Lamé's two moduli of elasticity by

$$Y = \mu\frac{(3\lambda + 2\mu)}{(\lambda + \mu)}\overset{\lambda=\mu}{=} 2.5\mu. \tag{13}$$

If l_P denotes the dimension of the FCC elementary cell that consists of the four interacting Planck particles showing the mass m_P, the Planck density equals: $\rho_P = 4m_P/l_P^3$ = const. The computed Planck density, the Young's modulus and the other properties of the Cauchy continuum at the Planck scale are shown in Table 1. We consider the small deformation limit and the negligible density changes. It allows us to assume the constant transverse wave velocity: $c = \sqrt{\mu/\rho_P} = \mathrm{const}$ [31] and Equation (11) becomes:

$$\frac{1}{c^2}\frac{\partial^2\boldsymbol{u}}{\partial t^2} = 3\mathrm{grad\,div}\boldsymbol{u} - \mathrm{rot\,rot}\boldsymbol{u} + \frac{1}{\mu}\boldsymbol{F}. \tag{14}$$

Table 1
The physical constants of the Cauchy continuum (FCC ideal isotropic crystal)

Label used in this work	Planck constants	Symbol for unit	Value	SI unit	Reference
Lattice parameter	Planck length	l_P	$1.616229(38) \times 10^{-35}$	m	[34]
Poisson ratio	–	ν	0.25	–	[32]
Mass of the Planck particle	Planck mass	m_P	$2.176470(51) \times 10^{-8}$	kg	[34]
Duration of the internal process	Planck time	t_P	$5.39116(13) \times 10^{-44}$	s^{-1}	[34]
Transverse wave velocity	Light velocity in vacuum	$c = \frac{l_P}{t_P}$	2.99792458×10^8	$m \cdot s^{-1}$	[34]
Planck density	–	ρ_P	2.062072×10^{97}	$kg \cdot m^{-3}$	[34]
Young's modulus Intrinsic energy density	–	$Y = 2.5\rho_P c^2$	$4.6332447 \times 10^{114}$	$kg \cdot m^{-1} \cdot s^{-2}$	[34]

The Cauchy model (and to the same degree the majority of physical problems) cannot be reduced to vectorial models (the vector product does not permit the formulation of algebra with unity, for example, the division operation is not defined). By acting on Equation (14) by rot and div operators we separate the transverse and the longitudinal processes:

$$\begin{gathered}\left.\begin{aligned}\operatorname{div}\left(\frac{1}{c^2}\frac{\partial^2\boldsymbol{u}}{\partial t^2}=3\nabla(\nabla\circ\boldsymbol{u})-\nabla\times(\nabla\times\boldsymbol{u})+\frac{1}{\mu}\boldsymbol{F}\right)\\ \operatorname{rot}\left(\frac{1}{c^2}\frac{\partial^2\boldsymbol{u}}{\partial t^2}=3\nabla(\nabla\circ\boldsymbol{u})-\nabla\times(\nabla\times\boldsymbol{u})+\frac{1}{\mu}\boldsymbol{F}\right)\end{aligned}\right\}\Rightarrow\\ \underset{\nabla\times(\nabla\times\boldsymbol{u}_\phi)=-\Delta\boldsymbol{u}_\phi}{\Rightarrow}\begin{cases}\dfrac{1}{c^2}\dfrac{\partial^2}{\partial t^2}\operatorname{div}\boldsymbol{u}_0=3\Delta\operatorname{div}\boldsymbol{u}_0+\dfrac{1}{\mu}\operatorname{div}\boldsymbol{F}\\ \dfrac{1}{c^2}\dfrac{\partial^2}{\partial t^2}\operatorname{rot}\boldsymbol{u}_\phi=\Delta\operatorname{rot}\boldsymbol{u}_\phi+\dfrac{1}{\mu}\operatorname{rot}\boldsymbol{F},\end{cases}\end{gathered}\tag{15}$$

where $\boldsymbol{u}=\boldsymbol{u}_0+\boldsymbol{u}_\phi$, $\operatorname{rot}\boldsymbol{u}_0=0$, $\operatorname{div}\boldsymbol{u}_\phi=0$. The Cauchy equation of motion combined with the Helmholtz decomposition theorem results in four second-order scalar differential equations, "quattro cluster", and implies the transverse and longitudinal waves in the Cauchy elastic solid.

Remark 2

1. *The mathematical analysis confirms that the Cauchy model is well posed, i.e., it has a unique solution and its behavior changes continuously with respect to the initial conditions* [30].
2. *The Helmholtz decomposition is never unique* [35].
3. *The Hamilton algebra of quaternions and its relation to the four-dimensional space allow combining the Cauchy theory with the electrodynamics, gravity and quantum mechanics.*

2. THEORY

2.1. The Cauchy deformation field in the quaternion representation

The Cauchy classical theory of elasticity is an elegant starting point to show the physical reality and the significance and beauty of quaternions. The Hamilton algebra $\mathbb{H}$ allows the recoupling of compression and twist that are separated in (15). Upon denoting $\sigma_0=\operatorname{div}\boldsymbol{u}_0=(\sigma_0,0,0,0)$ and $\hat{\phi}=\operatorname{rot}\boldsymbol{u}_\phi=(0,\phi_1,\phi_2,\phi_3)$ we get

$$\begin{cases}\dfrac{\partial^2\sigma_0}{\partial t^2}=3c^2\Delta\sigma_0\\ \dfrac{\partial^2\hat{\phi}}{\partial t^2}=c^2\Delta\hat{\phi}\end{cases}\Leftrightarrow\left(\frac{\partial^2}{\partial t^2}-c^2\Delta\right)\sigma-2c^2\Delta\sigma_0=0.\tag{16}$$

The decomposition $\boldsymbol{u}=\boldsymbol{u}_0+\boldsymbol{u}_\phi$ in Equation (15) results in four equations in Equation (16) and implies the existence of the deformation field $\sigma=\sigma_0+\hat{\phi}$ that represents the twist and compression fields as a superposition of real (scalar compression σ_0) and imaginary (twist vector $\hat{\phi}$) field parts at each point

$$\sigma=\sigma_0+\hat{\phi}\in\mathbb{H}\quad\text{and}\quad\sigma^*=\sigma_0-\hat{\phi}\in\mathbb{H}.\tag{17}$$

Adding equations in (16) one gets the quaternion form of the Cauchy motion equation

$$\frac{1}{c^2}\frac{\partial^2\sigma}{\partial t^2}-\Delta\sigma-2\Delta\sigma_0=0.\tag{18}$$

Since $\dot{\boldsymbol{u}}\circ\dot{\boldsymbol{u}}=\hat{u}\circ\hat{u}=-\hat{u}\cdot\hat{u}=\hat{u}\cdot\hat{u}^*$, where $\hat{u}=\dot{u}_1 i+\dot{u}_2 j+\dot{u}_3 k$ and $\dot{\boldsymbol{u}}=(\dot{u}_1,\dot{u}_2,\dot{u}_3)$, the overall energy of the deformation field Relation (12) takes the form:

$$e=\frac{1}{2}\hat{\dot{u}}\cdot\hat{\dot{u}}^*+\frac{1}{2}c^2\,\sigma\cdot\sigma^*+c^2\sigma_0^2,\tag{19}$$

where the velocity within the particle wave is given by the Cauchy–Riemann derivative

$$\hat{\dot{u}}=-\frac{\hbar}{m}D\sigma,\tag{20}$$

where $D\sigma=\operatorname{grad}\sigma_0+\operatorname{rot}\hat{\phi}$ because $\operatorname{div}\hat{\phi}=\operatorname{div}\operatorname{rot}\boldsymbol{u}_\phi=0$. The overall energy in an arbitrary volume Ω follows from Equation (19):

$$\begin{aligned}E&=\int_\Omega\rho_E(t,x)dx=\\ &=\int_\Omega\rho_P\left(\frac{1}{2}\hat{\dot{u}}\cdot\hat{\dot{u}}^*+\frac{1}{2}c^2\,\sigma\cdot\sigma^*+c^2\sigma_0^2\right)dx=mc^2,\end{aligned}\tag{21}$$

where the external potential, e.g., $V(x)$, is omitted.

The kinetic energy in (19) follows from the vectorial form: $\hat{u}\cdot\hat{u}^*/2$, that can be regarded as $\mathbb{R}^3$ representation that does not describe the volume changes. Contrary, the deformations have quaternion representation in $\mathbb{R}^4$. In (17) the quaternion potential, i.e., the deformation four-potential, is defined by:

$$\begin{array}{ccccc}\sigma & = & \sigma_0 & + & \hat{\phi}.\\ \begin{bmatrix}q\text{-potential,}\\ \text{deformation}\end{bmatrix} & = & \begin{bmatrix}\operatorname{div}\boldsymbol{u}_0\\ \text{compression}\end{bmatrix} & + & \begin{bmatrix}\operatorname{rot}\boldsymbol{u}_\phi\\ \text{twist}\end{bmatrix}\end{array}\tag{22}$$

The quaternionic velocity $\dot{u}\in\mathbb{H}$ should represent now all the deformation velocities in $\mathbb{R}^4$. In the derivation of the first order quaternion PDEs and in the electron model (Sections 2.6 and 3) we demonstrate the practical application with an example of the particle wave showing the equivalent mass m:

$$\begin{array}{ccccc}\dot{u} & = & \dot{u}_0 & + & \hat{\dot{u}}\\ & & -\dfrac{\hbar}{m}\dfrac{\sigma_0}{l_P} & - & \dfrac{\hbar}{m}(\operatorname{grad}\sigma_0+\operatorname{rot}\hat{\phi}).\\ \begin{bmatrix}\text{velocity of the}\\ q\text{-potential changes}\\ \text{deformation velocity}\end{bmatrix} & = & \begin{bmatrix}\text{compression}\\ \text{velocity}\end{bmatrix} & + & \begin{bmatrix}\text{twist velocity}\end{bmatrix}\end{array}\tag{23}$$

2.2. The boundary conditions

In order to obtain the boundary conditions we will find the flux S of the energy e. Let $V\subset\Omega$ be any subregion of Ω

with the smooth boundary ∂V. The rate of change of the total energy within V equals the negative of the net flux through ∂V:

$$\frac{d}{dt}\int_V e d^3\boldsymbol{r} = -\int_{\partial V} S \circ \boldsymbol{n} d(\partial V), \tag{24}$$

where $\boldsymbol{n} = (n_1, n_2, n_3) \in \mathbb{R}^3$ is the outside normal unit vector to ∂V. It follows from the Gauss theorem that

$$\int_V \frac{\partial e}{\partial t} d^3\boldsymbol{r} = -\int_V \operatorname{div} S d^3\boldsymbol{r}. \tag{25}$$

Thus

$$\frac{\partial e}{\partial t} = -\operatorname{div} S \tag{26}$$

as V was arbitrary.

On the other hand Formula (12) upon differentiation becomes:

$$\frac{\partial e}{\partial t} = \dot{\boldsymbol{u}} \circ \ddot{\boldsymbol{u}} + 3c^2 \operatorname{div}\boldsymbol{u} \operatorname{div}\dot{\boldsymbol{u}} + c^2 \operatorname{rot}\boldsymbol{u} \circ \operatorname{rot}\dot{\boldsymbol{u}} \tag{27}$$

and using Equation (14) with $\boldsymbol{F} = 0$ we have

$$\frac{\partial e}{\partial t} = \dot{\boldsymbol{u}} \circ (3c^2 \operatorname{grad}\operatorname{div}\boldsymbol{u} - c^2 \operatorname{rot}\operatorname{rot}\boldsymbol{u}) + 3c^2 \operatorname{div}\boldsymbol{u} \operatorname{div}\dot{\boldsymbol{u}} + \\ + c^2 \operatorname{rot}\boldsymbol{u} \circ \operatorname{rot}\dot{\boldsymbol{u}}. \tag{28}$$

Taking into account the identities $\operatorname{div}(a\boldsymbol{A}) = \boldsymbol{A} \circ \operatorname{grad} a + a \operatorname{div}\boldsymbol{A}$ and $\operatorname{div}(\boldsymbol{A} \times \boldsymbol{B}) = \boldsymbol{B} \circ \operatorname{rot}\boldsymbol{A} - \boldsymbol{A} \circ \operatorname{rot}\boldsymbol{B}$, Formula (28) becomes:

$$\frac{\partial e}{\partial t} = -\operatorname{div}\left[c^2(\operatorname{rot}\boldsymbol{u}) \times \dot{\boldsymbol{u}} - 3c^2(\operatorname{div}\boldsymbol{u})\dot{\boldsymbol{u}}\right]. \tag{29}$$

Comparing (26) and (29), the energy flux equals $S = c^2(\operatorname{rot}\boldsymbol{u}) \times \dot{\boldsymbol{u}} - 3c^2(\operatorname{div}\boldsymbol{u})\dot{\boldsymbol{u}}$ or in the quaternionic notation

$$\hat{S} = c^2\hat{\phi} \times \hat{u} - 3c^2\sigma_0\hat{u} \tag{30}$$

or equivalently

$$\hat{S} = c^2(\sigma - \sigma_0) \times \hat{u} - 3c^2\sigma_0\hat{u}. \tag{31}$$

Thus, Relation (29) can be written in the form of the quaternionic continuity equation

$$\frac{\partial e}{\partial t} + \operatorname{div}\hat{S} = 0. \tag{32}$$

Because nothing flows over the boundary $\partial\Omega$, we assume that

$$\hat{S} \circ \hat{n} = 0 \tag{33}$$

on $\partial\Omega$, where $\hat{n} = n_1 i + n_2 j + n_3 k$. Equation (33) will be used in the construction of the boundary conditions of an electron model.

2.3. Maxwell equations in the Cauchy continuum

In this section we will show that the Cauchy equation implies the Maxwell equations. We consider System (15) with the nonzero external force field $\boldsymbol{F}$:

$$\begin{cases} \dfrac{1}{c^2}\dfrac{\partial^2}{\partial t^2}\operatorname{div}\boldsymbol{u}_0 - 3\Delta\operatorname{div}\boldsymbol{u}_0 = \dfrac{1}{\mu}\operatorname{div}\boldsymbol{F} \\ \dfrac{1}{c^2}\dfrac{\partial^2}{\partial t^2}\operatorname{rot}\boldsymbol{u}_\phi - \Delta\operatorname{rot}\boldsymbol{u}_\phi = \dfrac{1}{\mu}\operatorname{rot}\boldsymbol{F}. \end{cases} \tag{34}$$

The force $\boldsymbol{F}$ is due to the deformations $\operatorname{div}\boldsymbol{u}$ and $\operatorname{rot}\boldsymbol{u}$ caused by the presence of the flux of the external charged particles, i.e., there exists the external displacement field

$$f = f_0 + \hat{f} \in \mathbb{H}. \tag{35}$$

The force field follows from the Cauchy–Riemann derivative and the condition $\operatorname{div}\hat{f} = 0$:

$$\boldsymbol{F} = -\mu Df = -\mu \operatorname{grad} f_0 - \mu \operatorname{rot}\hat{f}. \tag{36}$$

Combining (34), (36) and the definitions in (22), System (34) becomes:

$$\begin{cases} \dfrac{1}{c^2}\dfrac{\partial^2\sigma_0}{\partial t^2} - 3\Delta\sigma_0 = -\Delta f_0 \\ \dfrac{1}{c^2}\dfrac{\partial^2\hat{\phi}}{\partial t^2} - \Delta\hat{\phi} = \Delta\hat{f}. \end{cases} \tag{37}$$

By noting that the negative f_0 is a result of net inflow of charged particles and it results in the positive change of σ_0 we get: $\Delta f_0 - \Delta\sigma_0 = 0$, System (37) becomes structurally symmetric:

$$\begin{cases} \dfrac{1}{c^2}\dfrac{\partial^2\sigma_0}{\partial t^2} - \Delta\sigma_0 = \Delta f_0 \\ \dfrac{1}{c^2}\dfrac{\partial^2\hat{\phi}}{\partial t^2} - \Delta\hat{\phi} = \Delta\hat{f}. \end{cases} \tag{38}$$

Upon adding equations in (38) one gets quaternionic representation of the Maxwell displacements

$$\left(\frac{1}{c^2}\frac{\partial^2}{\partial t^2} - \Delta\right)(\sigma_0 + \hat{\phi}) = \Delta(f_0 + \hat{f}). \tag{39}$$

Introducing the Maxwell potential definitions: $\varphi = \sigma_0 = \operatorname{div}\boldsymbol{u}_0$ and $\boldsymbol{A} = \hat{\phi} = \operatorname{rot}\boldsymbol{u}_\phi$ where they denote the irrotational scalar and solenoidal vector potentials, we get the four-potential and flux:

$$A = \varphi + \boldsymbol{A} = \varphi + A_1 i + A_2 j + A_3 k, \tag{40}$$

$$\mu J = J_0 + \hat{J} = -\Delta f_0 - \Delta\hat{f} = -\Delta f. \tag{41}$$

The macroscopic version of the Maxwell equations is Formula (39) with the use of (40) and (41):

$$\left(-\frac{1}{c^2}\frac{\partial^2}{\partial t^2} + \Delta\right)A = \mu J. \tag{42}$$

The microscopic empty space version is as follows. Consider the empty crystal space (without the charged particles) and the irrotational deformations are negligible: $J = 0$. Consequently Relation (42) reduces to

$$\frac{1}{c^2}\frac{\partial^2 \boldsymbol{A}}{\partial t^2} + \text{rot rot}\,\boldsymbol{A} = 0, \tag{43}$$

by the postulate $\varphi = 0$, $\text{div}\,\boldsymbol{A} = 0$. We introduce the definitions:

$$\boldsymbol{E} := -\frac{1}{c}\frac{\partial \boldsymbol{A}}{\partial t}, \tag{44}$$

$$\boldsymbol{H} := \text{rot}\,\boldsymbol{A}. \tag{45}$$

Upon combining (43)–(45) and by taking the rotation in Definition (44): $\text{rot}\,(c^{-1}(\partial \boldsymbol{A}/\partial t)) = -\,\text{rot}\,\boldsymbol{E}$ the Maxwell system for vacuum follows:

$$\begin{cases} \dfrac{1}{c}\dfrac{\partial \boldsymbol{E}}{\partial t} - \text{rot}\,\boldsymbol{H} = 0 \\ \dfrac{1}{c}\dfrac{\partial \boldsymbol{H}}{\partial t} + \text{rot}\,\boldsymbol{E} = 0. \end{cases} \tag{46}$$

2.4. Bosons, fermions, quarks and their *q*-potentials

The quaternionic propagators

The coupling of the transverse and the longitudinal waves takes place in the elementary cell of the Cauchy continuum, i.e., at the Planck scale. The quaternionic oscillator controls the acceleration of all the *q*-potential components during the propagation, e.g., in the particle wave in Ω: $\ddot{\sigma}_0$, $\ddot{\phi}_1$, $\ddot{\phi}_2$, $\ddot{\phi}_3$. The function $G_0 \in \mathbb{R}$ will be called the frequency of the oscillator. In the earlier papers, we disregarded that the twists ϕ_1, ϕ_2 and ϕ_3 form the twist vector $\hat{\phi} = \phi_1 i + \phi_2 j + \phi_3 k$ [35] and are controlled by the oscillator G_0. Thus, the relation between the *q*-potential and its scalar component σ_0 will be corrected and consider the two *q*-potential constituents, σ_0 and $\hat{\phi}$ [35]:

$$\left\langle \frac{\partial^2 \sigma}{\partial t^2} \right\rangle = 2\left\langle \frac{\partial^2 \sigma_0}{\partial t^2} \right\rangle = 8\pi^2 f_P f, \tag{47}$$

and the frequency of the quaternionic oscillator equals

$$G_0(f) = 8\pi^2 f_P f. \tag{48}$$

The particle wave frequency depends on the particle mass, $f = f(m)$, and follows from the $\mathbb{R}^1$ schema, e.g., see Figure 1 in [20]. The sum of moments of all the Planck masses forming the particle wave in Ω (at the arbitrary time t and solely due to the particle wave) equals the momentum of the particle m itself. On the other hand, we may estimate the average momentum of the arbitrary single Planck mass m_P in the elementary cell during the whole particle cycle: $T = f^{-1}$. The complete cycle implies that every Planck mass m_P returns to its initial conditions: $\boldsymbol{u}_P(t) = \boldsymbol{u}_P(t + T)$ and $\dot{\boldsymbol{u}}_P(t) = \dot{\boldsymbol{u}}_P(t + T)$. The overall distance of the Planck mass during the wave cycle T equals $2\pi l_P$. Thus, the average momentum of the Planck mass $\bar{p}(m_P)$ during the particle wave cycle equals

$$\bar{p}(m_P) = m_P \frac{2\pi l_P}{T} = 2\pi m_P l_P f. \tag{49}$$

The momentum of the particle wave m results from the particle wave propagation velocity:

$$p(m) = mc. \tag{50}$$

Both moments must equal: $p(m) = \bar{p}(m_P)$, and the frequency of the particle wave becomes

$$f = \frac{mc}{2\pi m_P l_P}\frac{c}{c} = \frac{mc^2}{2\pi\hbar}, \quad \hbar = m_P c l_P, \tag{51}$$

where upon using the NIST data [36] for the Planck natural units m_P, l_P, t_P and the light velocity c, the constant $\hbar$ introduced in Relation (51) equals the Planck constant [17]. Combining Relations (48), (51) and the definition $f_P = 1/t_P$, the overall frequency of the quaternionic oscillator when the particle mass is known equals

$$G_0(m) = 4\pi\frac{mc^2}{\hbar t_P}. \tag{52}$$

The oscillator might generate the lower frequencies f of the particle wave and the families of propagators

$$G_n = \frac{1}{n}G_0(m) = \frac{1}{n}4\pi\frac{mc^2}{\hbar t_P}, \quad n \in \mathbb{N}, \tag{53}$$

where n can be interpreted as the measure of the propagator volume, e.g., $l_n = nl_P$.

The quaternionic oscillator $G_0(m)$ controls four propagators:

- the scalar I (spin 0), $G_0(m)\sigma \cdot \sigma^*$,
- the scalar II (spin 1/2), $G_0(m)\sigma_0$,
- the vectorial (spin 1/2), $G_0(m)\hat{\phi}$,
- the quaternionic (spin 1/2), $G_0(m)(\sigma_0 + \hat{\phi})$.

The above propagators generate the particle wave and simultaneously, the particles produce different force fields that are represented by the Poisson equation

$$nc^2\Delta\varphi + G_0(m)f = 0, \tag{54}$$

where φ and f are the quaternion valued functions.

Remark 3. *Substituting $mc^2 = E_0$ in (51), the Planck–Einstein relation follows: $E_0 = hf$, where $h = 2\pi\hbar$.*

The bosons

The family of the scalar second order PDE systems of the spin 0 particles results from the schema in (16) and (53). In (55), we show the core set of the three second order PDE and its equivalent, the set of two second order equations: the particle wave and the force field produced by the particle.

This schema can be written as

$$\begin{cases}\left(\dfrac{\partial^2}{\partial t^2}-c^2\Delta\right)\hat{\phi}=0\\ \left(\dfrac{\partial^2}{\partial t^2}-3c^2\Delta\right)\sigma_0=0\\ \left((n-1)\dfrac{\partial^2}{\partial t^2}-(n-3)c^2\Delta\right)\sigma_0+2G_0(m)\sigma\cdot\sigma^*=0\end{cases}\Leftrightarrow \tag{55}$$

$$\Leftrightarrow\begin{cases}\left(\dfrac{\partial^2}{\partial t^2}-c^2\Delta\right)\tilde{\sigma}_n+2G_0(m)\sigma\cdot\sigma^*=0\\ \left((n-1)\dfrac{\partial^2}{\partial t^2}-(n-3)c^2\Delta\right)\sigma_0+2G_0(m)\sigma\cdot\sigma^*=0,\end{cases}$$

where $\tilde{\sigma}_n = n\sigma_0 + \hat{\phi}$ and n denotes natural numbers. If $n = 1$, then System (55) results in [19]:

$$\begin{cases}\left(\dfrac{\partial^2}{\partial t^2}-c^2\Delta\right)\hat{\phi}=0\\ \left(\dfrac{\partial^2}{\partial t^2}-3c^2\Delta\right)\sigma_0=0\\ c^2\Delta\sigma_0+G_0(m)\sigma\cdot\sigma^*=0\end{cases}\Leftrightarrow \tag{56}$$

$$\Leftrightarrow\begin{cases}\left(\dfrac{\partial^2}{\partial t^2}-c^2\Delta\right)\sigma+2G_0(m)\sigma\cdot\sigma^*=0\\ c^2\Delta\sigma_0+G_0(m)\sigma\cdot\sigma^*=0.\end{cases}$$

The above two systems are equivalent and have five equations and five unknowns: σ_0, ϕ_1, ϕ_2, ϕ_3 and m. If mass m is unknown it may be treated as the parameter in the Poisson equation above. Equation (56) corresponds to the Klein–Gordon equation, i.e., the spin 0 boson particle.

The second order PDE Systems (55) and (56) comply with the Cauchy equation of motion, i.e., by adding the Poisson and wave equations, Equation (16) results.

The Poisson equation in (56) describes the potential σ_0 of the deformation field

$$c^2\Delta\sigma_0=-G_0(m)\sigma\cdot\sigma^*=-4\pi\frac{mc^2}{\hbar t_P}\sigma\cdot\sigma^*. \tag{57}$$

It can be expressed as a function of the particle mass density $\rho = (m\sigma\cdot\sigma^*)/l_P^3$:

$$c^2\Delta\sigma_0=-4\pi\rho\frac{l_P^3}{m_P t_P^2}=-4\pi\rho G. \tag{58}$$

Using the data in Table 1, the gravitational constant equals: $G = l_P^3/t_P^2 m_P = 6.674082 \times 10^{-11}\ \mathrm{m^3\cdot kg^{-1}\cdot s^{-2}}$. The particle mass center equals its wave energy center. The "space-localized" particle is defined in the sense given by the Bodurov definition [37]:

A singularity-free multi-component function $\sigma = (\sigma_0, \phi_1, \phi_2, \phi_3) \in \mathbb{H}$ *of the space* $x = (x_1, x_2, x_3)$ *and time t variables will be called space-localized if* $\|\sigma(t, x)\|_E \to 0$ *sufficiently fast when* $\|x\|_E \to \infty$ *for each t, so that its Hermitean norm*:

$$\left\|\sigma\right\|^2=\langle\sigma,\sigma^*\rangle=\int_\Omega\left(\sigma_0^2+\sum_{l=1}^{3}\phi_l\cdot\phi_l^*\right)dx=\int_\Omega\sigma\cdot\sigma^*dx<\infty \tag{59}$$

remains finite for all time.

The particles formed by the odd number of quarks

The strong coupling is considered in the further sections: $n = 1$ in Relation (53).

We begin with the vectorial potential, where the term $G_0(m)\ \hat{\phi}$ fixes the density of the rate of twist change and is called vectorial propagator:

$$\begin{cases}\left(\dfrac{\partial^2}{\partial t^2}-c^2\Delta\right)\hat{\phi}=0\\ \left(\dfrac{\partial^2}{\partial t^2}-3c^2\Delta\right)\sigma_0=0\\ -c^2\Delta\hat{\phi}+G_0(m)\hat{\phi}=0\end{cases}\Leftrightarrow\begin{cases}\left(\dfrac{\partial^2}{\partial t^2}-3c^2\Delta\right)\sigma+2G_0(m)\hat{\phi}=0\\ -c^2\Delta\hat{\phi}+G_0(m)\hat{\phi}=0.\end{cases} \tag{60}$$

Upon the rearrangement, the particle wave (electron) and the vectorial Poisson equations are evident. The adding equations in System (60) shows that it complies with the Cauchy equation of motion (16):

$$\begin{cases}\left(\dfrac{\partial^2}{\partial t^2}-3c^2\Delta\right)\sigma+2G_0(m)\hat{\phi}=0,\\ -c^2\Delta\hat{\phi}+G_0(m)\hat{\phi}=0,\end{cases}\Rightarrow \tag{61}$$

$$\Rightarrow\left(\frac{\partial^2}{\partial t^2}-c^2\Delta\right)\sigma-2c^2\Delta\sigma_0=0.$$

Note that the wave propagation velocity in System (60) equals the velocity of longitudinal waves in the Cauchy continuum: $c_L=\sqrt{3}c$ [17]. The vectorial Poisson equation in (60) confirms that it is the second order PDE system for electron. The quaternion propagator, $G_0(m)(\sigma_0 + \hat{\phi})$, the vectorial, $G_0(m)\hat{\phi}$, and scalar, $G_0(m)\sigma_0$, propagators are "merged" and form a strongly coupled system. The rearrangement of System (62) is shown below and displays different forms of the second order PDE systems:

$$\begin{cases}\left(\dfrac{\partial^2}{\partial t^2}-c^2\Delta\right)\hat{\phi}=0\\ \left(\dfrac{\partial^2}{\partial t^2}-3c^2\Delta\right)\sigma_0=0\\ -c^2\Delta\hat{\phi}+G_0(m)\hat{\phi}=0\\ c^2\Delta\sigma_0+G_0(m)\sigma_0=0\end{cases}\Leftrightarrow\begin{cases}\left(\dfrac{\partial^2}{\partial t^2}-c^2\Delta\right)\hat{\phi}=0\\ \left(\dfrac{\partial^2}{\partial t^2}-3c^2\Delta\right)\sigma_0=0\\ c^2\Delta(\sigma_0-\hat{\phi})+G_0(m)(\sigma_0+\hat{\phi})=0\end{cases}\Leftrightarrow \tag{62}$$

$$\Leftrightarrow\begin{cases}\left(\dfrac{\partial^2}{\partial t^2}2c^2\Delta\right)\sigma+G_0(m)(\sigma_0+\hat{\phi})=0\\ c^2\Delta\sigma^*+G_0(m)\sigma=0.\end{cases}$$

The comparison of the scalar, vectorial and quaternionic propagators shows that the *q*-propagator offers the strongest coupling, Equation (62). The quaternionic Poisson equation in (62) reveals that it is the second order PDE system for proton. The sum of equations in (62) shows that system complies with the Cauchy equation (16):

$$\begin{cases}\left(\frac{\partial^2}{\partial t^2}-2c^2\Delta\right)\sigma+G_0(m)(\sigma_0+\hat{\phi})=0\\ c^2\Delta(\sigma_0-\hat{\phi})+G_0(m)(\sigma_0+\hat{\phi})=0\end{cases}\Rightarrow$$
$$\Rightarrow\left(\frac{\partial^2}{\partial t^2}-c^2\Delta\right)\sigma-2c^2\Delta\sigma_0=0. \tag{63}$$

Note that the propagation velocity in System (62) exceeds the transverse wave velocity $c'=\sqrt{2}c$.

The quarks

The comparison of Systems (56), (60) and (62) allows for the postulation of second order PDE for the quarks from the *up* and *down* groups. Specifically, the second order system of the *u* quark from the *up* group equals:

$$\begin{cases}\left(\frac{1}{3}\frac{\partial^2}{\partial t^2}-c^2\Delta\right)\sigma+\frac{2}{3}G_0(m)\hat{\phi}=0\\ -c^2\frac{2}{3}\Delta\hat{\phi}-\frac{2}{3}G_0(m)\hat{\phi}=0\end{cases} \tag{64}$$

and the system of the *d* quark from the *down* group

$$\begin{cases}\frac{1}{3}\frac{\partial^2\sigma}{\partial t^2}+G_0(m)\sigma_0-\frac{1}{3}G_0(m)\hat{\phi}=0\\ c^2\Delta\left(\sigma_0+\frac{1}{3}\hat{\phi}\right)-G_0(m)\left(\sigma_0-\frac{1}{3}\hat{\phi}\right)=0.\end{cases} \tag{65}$$

The sum of equations in the above quark Systems (64) and (65) does not comply with the Cauchy equation of motion (16) and may indicate their short lifetime. The terms $2/3(G_0(\mathrm{m})\hat{\phi})$ and $-1/3(G_0(\mathrm{m})\hat{\phi})$ in Systems (64) and (65) respectively, are related to the charge (Table 2).

Table 2
The basic properties of the quarks in baryons

Group	Quarks	Charge	Spin
up	*u, c, t*	2/3	1/2
down	*d, s, b*	–1/3	1/2

There are two groups of hadrons: baryons (containing three quarks or three antiquarks); and mesons (containing the quark and an antiquark). In the following we show that Systems (60)–(65) comply with the experimental findings shown in Table 2.

The proton is formed be the two up and the single down quarks: *d* – *u* – *u*. Thus by computing the sum of two Systems (64) and one System (65) we may expect the proton, System (62):

$$\begin{cases}\frac{1}{3}\frac{\partial^2\sigma}{\partial t^2}+G_0(m)\sigma_0-\frac{1}{3}G_0(m)\hat{\phi}=0\\ c^2\Delta\left(\sigma_0+\frac{1}{3}\hat{\mathrm{f}}\right)+G_0(m)\left(\sigma_0-\frac{1}{3}\hat{\phi}\right)=0\end{cases}+$$
$$+2\begin{cases}\left(\frac{1}{3}\frac{\partial^2}{\partial t^2}-c^2\Delta\right)\sigma+\frac{2}{3}G_0(m)\hat{\phi}=0\\ -c^2\frac{2}{3}\Delta\hat{\phi}+\frac{2}{3}G_0(m)\hat{\phi}=0\end{cases} \tag{66}$$

and the result is identical with Equations (62):

$$\begin{cases}\left(\frac{\partial^2}{\partial t^2}-2c^2\Delta\right)\sigma+G_0(m)(\sigma_0+\hat{\phi})=0\\ c^2\Delta(\sigma_0-\hat{\phi})+G_0(m)(\sigma_0+\hat{\phi})=0.\end{cases} \tag{67}$$

The neutron is formed by the one up and the two down quarks: *d* – *d* – *u*:

$$2\times\begin{cases}\frac{1}{3}\frac{\partial^2\sigma}{\partial t^2}+G_0(m)\sigma_0-\frac{1}{3}G_0(m)\hat{\phi}=0\\ c^2\Delta\left(\sigma_0+\frac{1}{3}\hat{\phi}\right)+G_0(m)\left(\sigma_0-\frac{1}{3}\hat{\phi}\right)=0\end{cases}+$$
$$+\begin{cases}\left(\frac{1}{3}\frac{\partial^2}{\partial t^2}-c^2\Delta\right)\sigma+\frac{2}{3}G_0(m)\hat{\phi}=0\\ -c^2\frac{2}{3}\Delta\hat{\phi}+\frac{2}{3}G_0(m)\hat{\phi}=0\end{cases} \tag{68}$$

and the result is in agreement with neutron System (56):

$$\begin{cases}\frac{\partial^2\sigma}{\partial t^2}-c^2\Delta\sigma+2G_0(m)\sigma_0=0\\ c^2\Delta\sigma_0+G_0(m)\sigma_0=0.\end{cases} \tag{69}$$

Systems (60), (67) and (69) represent coupled second order PDE's and show the different coupling strengths. The strongest coupling of the proton is related to its enormously long lifetime, Equation (67).

2.5. The quaternionic Schrödinger equation

The vectorial Poisson equation indicates that it is the second order PDE system for an electron. We will apply the schema in System (60) in the integral form of the energy conservation, in Equation (21). We treat the wave as a particle in an arbitrary volume Ω [19]. The energy per mass unit

$$e=\frac{1}{2}\hat{u}\cdot\hat{u}^*+\frac{3}{2}c^2\sigma\cdot\sigma^*-c^2\hat{\phi}\cdot\hat{\phi}^* \tag{70}$$

in the volume occupied by the particle wave defines its overall energy

$$E_O=E_p+E_V=\int_\Omega\rho_p e dx, \tag{71}$$

where E_p and E_V are energies of the particle and of its force field respectively, ρ_p is the Planck mass density.

The first step in deriving the Schrödinger equation is the choice of the symmetric formula scheme for the particle energy, E_p. Equation (71) can be written in the equivalent form the following schema in System (60). We separate the E_p and E_V terms in the integral formula

$$E_p + E_V = \rho_P \int_\Omega \left(\frac{1}{2}\hat{u}\cdot\hat{u}^* + \frac{3}{2}c^2\sigma\cdot\sigma^* - c^2\hat{\phi}\cdot\hat{\phi}^* \right) dx \Leftarrow$$
$$\Leftarrow \begin{cases} E_p = \frac{1}{2}\rho_P \int_\Omega (\hat{u}\cdot\hat{u}^* + 3c^2\sigma\cdot\sigma^*)dx \\ E_V = \rho_P \int_\Omega (-c^2\hat{\phi}\cdot\hat{\phi}^*)dx. \end{cases} \tag{72}$$

The mass of the particle $m = E_p/c^2$ follows from the particle wave energy in (72):

$$m = \frac{1}{2}\rho_P \int_\Omega \left(3\sigma\cdot\sigma^* + \frac{\hat{u}\cdot\hat{u}^*}{c^2} \right) dx. \tag{73}$$

The terms $3\sigma \cdot \sigma^*$ and $\hat{u} \cdot \hat{u}^*/c^2$ oscillate and depend on the time and position. The symmetric structure of (73) allows normalizing the deformation and mass velocity with respect to the overall particle mass:

$$\begin{aligned} &\int_\Omega \frac{3\rho_P}{m}\sigma\cdot\sigma^* dx = \int_\Omega \psi\cdot\psi^* dx = 1, \text{ where } \psi = \sqrt{\frac{3\rho_P}{m}}\sigma, \\ &\int_\Omega \frac{\rho_P}{mc^2}\hat{u}\cdot\hat{u}^* dx = \int_\Omega \psi\cdot\psi^* dx = 1, \text{ where } \psi = \sqrt{\frac{\rho_P}{m}}\frac{\hat{u}}{c}. \end{aligned} \tag{74}$$

The quaternionic particle mass density ψ can be called the quaternionic probability because the relation $\int_\Omega \psi\cdot\psi^* dx = 1$ in (74) is satisfied. Obviously, the terms $\psi = \sqrt{(3\rho_P/m)}\sigma$ and $\psi \cdot \psi^*$ vary in time.

We analyze the evolution of the wave as in Relations (73) and (74) in the time-invariant potential field, e.g., the particle wave in the field generated by other particles. The overall particle energy is now a sum of the ground and excess energy Q:

$$E = E_p + Q = \int_\Omega \left(\frac{3}{2}\rho_P c^2\sigma\cdot\sigma^* + \frac{1}{2}\rho_P\hat{u}\cdot\hat{u}^* + V(x)\psi\cdot\psi^* \right) dx. \tag{75}$$

We consider the low excess energies, and the impact of Q on the overall particle mass in (74) is marginal. Thus, Relation (75) becomes:

$$\begin{aligned} E = E_p + Q &= \int_\Omega \left(\frac{1}{2}mc^2\psi\cdot\psi^* + \frac{1}{2}\rho_P\hat{u}\cdot\hat{u}^* + V(x)\psi\cdot\psi^* \right) dx = \\ &= \frac{1}{2}mc^2 + \int_\Omega \left(\frac{1}{2}\rho_P\hat{u}\cdot\hat{u}^* + V(x)\psi\cdot\psi^* \right) dx. \end{aligned} \tag{76}$$

Both the E_p and m are constant, thus it is enough to minimize the relation

$$Q = \int_\Omega \left(\frac{1}{2}\rho_P\hat{u}\cdot\hat{u}^* + V(x)\psi\cdot\psi^* \right) dx. \tag{77}$$

The above relation contains two unknowns: $\hat{u} = \partial u/\partial t$ and ψ. By relating the local lattice velocity $\hat{u}$ to the force, specifically to the normalized Cauchy–Riemann derivative of the deformation $l_P D\sigma$, one gets

$$\hat{u} = \frac{\hat{p}}{m} = -\frac{\hbar}{m}D\sigma. \tag{78}$$

By introducing (78) and the normalization (74), Relation (77) generates the functional:

$$Q[\psi] = \int_\Omega \left(\frac{\hbar^2}{2m}(D\psi)\cdot(D\psi)^* + V(x)\psi\cdot\psi^* \right) dx. \tag{79}$$

The functional $Q[\psi]$, Equation (79), was minimized with respect to a quaternion function, such that ψ satisfies the normalization introduced in the relation. One may follow the schema used in [19]. In simple terms, we seek a differential equation that has to be satisfied by the ψ function to minimize the energies allowed by (79). Given the functional (79), the conditional extreme is found using the Lagrange coefficients method and the Du Bois–Reymond variational lemma [38]. In such a case, ψ satisfies the time-invariant Schrödinger equation satisfied by the particle wave in the ground state of the energy E [19]:

$$-\frac{\hbar^2}{2m}\Delta\psi + V(x)\psi = \lambda\psi, \tag{80}$$

where a constant factor on the right-hand side can be considered as extra energy of the particle in the presence of the field $V = V(x)$. For $E = \lambda$, Equation (80) is clearly the time-independent Schrödinger equation satisfied by the particle in the ground state of the energy E:

$$-\frac{\hbar^2}{2m}\Delta\psi + V(x)\psi = E\psi. \tag{81}$$

2.6. The first order PDE in the Cauchy continuum

The operator quantum mechanics is based on the complex number algebra and matrix algebra. The canonical quantization starts from the classical mechanics and assumes that the point particle is described by a "probabilistic wave function". Dirac applied complex combinations of the displacements and velocities in the linear problem of secondary quantization [39] and replaced the second order Klein–Gordon equation by an array of first order equations. He recognized the problem of medium for the transmission of waves:

It is necessary to set up an action principle and to get a Hamiltonian formulation of the equations suitable for quantization purposes, and for this the aether velocity is required [39].

In this section we follow the Dirac concept. We derive the formulae based on the aether concept, specifically the Cauchy continuum and the quaternionic oscillator $G_\lambda(m)$ for the first order PDE and the separated Planck time scale. The

second order particle wave equation, e.g., in the electron PDE System (61), contains two parts:

$$\begin{array}{ccc} \left(\frac{\partial^2}{\partial t^2} - c_L^2\Delta\right)\sigma & + & \\ \left[\begin{array}{c}\text{second order wave term } \sigma^{\mu}\sigma_{\mu}\text{: variable} \\ \sigma \text{ and constant wave velocity } c_L = \sqrt{3}c\end{array}\right] & + & \\ + \quad 2G_0(m)\hat{\phi} & = & 0. \\ + \quad \left[\begin{array}{c}\text{Propagator with oscillator } G_0(m) \\ \text{that runs at two frequencies}\end{array}\right] & = & 0 \end{array} \tag{82}$$

We will comply with above schema for the first order PDE:

$$\begin{array}{ccc} \frac{\partial \dot{u}}{\partial t} - c_L D\hat{u} & + & \\ \left[\begin{array}{c}\text{First order wave term } \sigma_{\mu}\text{ : variable} \\ \dot{u}\text{, wave velocity } c_L = \sqrt{3}c\end{array}\right] & + & \\ + \quad 2G_{\lambda}(m)\hat{\dot{u}} & = & 0. \\ + \quad \left[\begin{array}{c}\text{Propagator with oscillator } G_{\lambda}(m) \\ \text{that runs at particle wave frequency}\end{array}\right] & = & 0 \end{array} \tag{83}$$

The first order wave term

We consider System (60) and the relation between the wave velocity and the Cauchy–Riemann derivative equation (78): $D\sigma = -(m/\hbar) \cdot \hat{u}$. The expression for the overall particle energy, Equation (72), implies:

- the deformation velocity as the alternative variable:

$$\dot{u} = \dot{u}_0 + \hat{\dot{u}}, \tag{84}$$

where $\dot{u}_0 = -(\hbar/m) \cdot (\sigma_0/l_p)$, $\hat{\dot{u}} = -(\hbar/m) \cdot D\sigma$,

- the longitudinal wave velocity as the wave propagation velocity:

$$c_L = \sqrt{3}c. \tag{85}$$

The motionless particle is considered, thus its wave is at a steady state. The second order time derivative of the q-potential in (83) we express as follows:

$$\frac{\partial^2\sigma}{\partial t^2} = \frac{\partial}{\partial t}\left(\frac{\partial\sigma}{\partial t}\right). \tag{86}$$

The term in the bracket on the right-hand side is the rate of the q-potential changes. We want to express this term by the new variable and separate the time scales. The rate of changes of the deformation potential $\partial\sigma/\partial t$ is due to the wave propagation within the particle space. The propagation process must follow the extremum principle, i.e., it is the brachistochrone problem [40]. The good example of "local principle" approximation is by Derbes [41].

We know that the wave path fulfills the extremum principle, i.e., the wave path follows its unique trajectory given by the Cauchy–Riemann derivative, $D\sigma$. The trajectory which has the minimum property globally in the whole volume Ω occupied by the particle must have the same property locally. This path grants the shortest possible travelling time for the waves identified in QQM. Considering $\sigma(\boldsymbol{u}(t, x))$ we get the formula

$$\frac{\partial\sigma}{\partial t} = \sum_{l=1}^{3}\frac{\partial\sigma}{\partial u_l}\frac{\partial u_l}{\partial t}.$$

Consequently from (84)–(86) we postulate the following:

$$\begin{cases} \frac{\partial u_l}{\partial t} = c \quad \Rightarrow \quad \frac{\partial\sigma}{\partial t} = \frac{mc_L}{\hbar}\dot{u} \\ \frac{\partial\sigma}{\partial u_l} = \frac{1}{\sqrt{3}}\frac{m}{\hbar}\dot{u} \end{cases} \tag{87}$$

for l = 1, 2, 3. From Relation (84) we get

$$D\sigma = -\frac{m}{\hbar}\hat{\dot{u}} \quad \Rightarrow \quad \Delta\sigma = -\mathrm{DD}\sigma = \frac{m}{\hbar}D\hat{\dot{u}}. \tag{88}$$

Combining Relations (87) and (88), we get the first order particle wave term consistent with the second order Formula (82):

$$\frac{\partial^2\sigma}{\partial t^2} - c_L^2\Delta\sigma = \frac{mc_L}{\hbar}\frac{\partial\dot{u}}{\partial t} - \frac{mc_L^2}{\hbar}D\hat{\dot{u}} = \frac{mc_L}{\hbar}\left(\frac{\partial\dot{u}}{\partial t} - c_L D\hat{\dot{u}}\right). \tag{89}$$

Thus, the first order particle wave term in (83) equals:

$$\frac{\partial\dot{u}}{\partial t} - c_L D\hat{\dot{u}} = 0. \tag{90}$$

The first order quaternionic oscillator

The frequency of the second order quaternionic oscillator results from two time scales in PK-C: $G_0(f) = 8\pi^2 f_P f$. We consider the macro scale only and first order PDE equation thus, by eliminating the Planck frequency from Relation (48), results in the frequency formula of the first order quaternionic oscillator when the particle mass is known:

$$G_{\lambda}(m) = 4\pi f = 2\frac{mc_L^2}{\hbar} = 6\frac{m}{m_P t_P}. \tag{91}$$

By introducing Relations (90) and (91) in the schema (83), the first order PDE for electron equals

$$\frac{\partial\dot{u}}{\partial t} - c_L D\hat{\dot{u}} - 12\frac{m}{m_P t_P}\hat{\dot{u}} = 0. \tag{92}$$

The electron spin

The energy Relations (72) are symmetrical and, in the case of the electron:

$$\begin{cases} E_{electron\ particle} = \frac{1}{2}\rho_P\int_{\Omega}(\hat{\dot{u}}\cdot\hat{\dot{u}}^{*} + c_L^2\sigma\cdot\sigma^{*})dx \\ E_{electron\ potential\ field} = \rho_P\int_{\Omega}(-c^2\hat{\phi}\cdot\hat{\phi}^{*})dx. \end{cases} \tag{93}$$

A particle is stable and its energy must be conserved. Thus, it is justified to assume that the constraint $\operatorname{div}\hat{\phi}=0$ holds for the completed particle cycle. In the static particle we postulate zero dissipation of the twist energy: $\operatorname{div}\hat{\phi}=0$. It implies the necessity of the spin, $\hat{S}$, the process that will provide the energy conservation:

$$\operatorname{div}\hat{\phi} = \operatorname{div}(\hat{\phi}+\hat{S}) = 0. \tag{94}$$

The equipartition of energy between the twists, $|\hat{\phi}| = |\hat{S}|$, implies the equipartition of moments: $|\hat{\phi}| = |\hat{S}|$. Thus, the overall momentum per mass unit equals: $2|\hat{S}| = \alpha$.

3. MATHEMATICAL MODEL OF AN ELECTRON

We consider the quaternionic system of equations shown in Equation (61):

$$\begin{cases} \dfrac{\partial^2\sigma}{\partial t^2} - 3c^2\Delta\sigma + 2G_0(m)\hat{\phi}=0 \\ c^2\Delta\hat{\phi} - G_0(m)\hat{\phi}=0. \end{cases} \tag{95}$$

System (95) is equivalent to the real hyperbolic-elliptic system

$$\begin{cases} \dfrac{\partial^2\sigma_0}{\partial t^2} - 3c^2\Delta\sigma_0 = 0 \\ \dfrac{\partial^2\hat{\phi}}{\partial t^2} - 3c^2\Delta\hat{\phi} + 2G_0(m)\hat{\phi}=0 \\ c^2\Delta\hat{\phi} - G_0(m)\hat{\phi}=0 \end{cases} \tag{96}$$

that can be written in the elegant mathematical form

$$\begin{cases} \dfrac{\partial^2\sigma_0}{\partial t^2} - 3c^2\Delta\sigma_0 = 0 \\ \dfrac{\partial^2\hat{\phi}}{\partial t^2} - c^2\Delta\hat{\phi}=0 \\ c^2\Delta\hat{\phi} - G_0(m)\hat{\phi}=0, \end{cases} \tag{97}$$

Each of the three equivalent Systems (95)–(97) obeys the constraints

$$\begin{cases} \operatorname{div}\hat{\phi}=0 \\ \phi_1 = 2\phi_2. \end{cases} \tag{98}$$

The energy must be conserved. Thus the flux, Equation (31), through the boundary must be zero and we consider the boundary condition in the form

$$(c^2\hat{\phi}\times\hat{u} - 3c^2\sigma_0\hat{u})\circ\hat{n} = 0, \tag{99}$$

where

$$\hat{u} = -\frac{\hbar}{m}(\nabla\sigma_0 + \operatorname{rot}\hat{\phi}). \tag{100}$$

Combining (99) and (100) results in

$$(-\hat{\phi}\times\nabla\sigma_0 - \hat{\phi}\times\operatorname{rot}\hat{\phi} + 3\sigma_0\nabla\sigma_0 + 3\sigma_0\operatorname{rot}\hat{\phi})\circ\hat{n} = 0. \tag{101}$$

An electron does not generate the scalar field and we add the condition

$$\nabla\sigma_0\circ\hat{n} = 0. \tag{102}$$

Consequently the condition (101) becomes

$$(\hat{\phi}\times\operatorname{rot}\hat{\phi} - 3\sigma_0\operatorname{rot}\hat{\phi})\circ\hat{n} = 0\,. \tag{103}$$

The twist $\hat{\phi}$ and compression σ_0 in the above differential problem (97) are only coupled at the boundary, Equation (103). In particular, σ_0 affects $\hat{\phi}$ but not vice versa. So, one may formulate two initial-boundary value problems.

3.1. Initial-boundary value problem for compression σ_0

The hyperbolic equation

$$\frac{\partial^2\sigma_0}{\partial t^2} - 3c^2\Delta\sigma_0 = 0 \tag{104}$$

with the Neumann boundary condition

$$\nabla\sigma_0\circ\hat{n} = 0 \tag{105}$$

and the initial conditions

$$\begin{cases} \sigma_0(0,x) = \sigma_{01}(x) \\ \dfrac{\partial\sigma_0}{\partial t}(0,x) = \sigma_{02}(x), \end{cases} \tag{106}$$

where the functions σ_{01} and σ_{02} are given.

3.2. Initial-boundary value problem for twist $\hat{\phi}$

The hyperbolic-elliptic system

$$\begin{cases} \dfrac{\partial^2\hat{\phi}}{\partial t^2} - c^2\Delta\hat{\phi}=0 \\ c^2\Delta\hat{\phi} - G_0(m)\hat{\phi}=0 \\ \operatorname{div}\hat{\phi}=0 \\ \phi_1 = 2\phi_2 \end{cases} \tag{107}$$

with the boundary condition

$$(\hat{\phi}\times\operatorname{rot}\hat{\phi} - 3\sigma_0\operatorname{rot}\hat{\phi})\circ\hat{n} = 0 \tag{108}$$

and the initial conditions

$$\begin{cases} \hat{\phi}(0,x) = \hat{\phi}_{01}(x) \\ \dfrac{\partial\hat{\phi}}{\partial t}(0,x) = \hat{\phi}_{02}(x), \end{cases} \tag{109}$$

where the functions $\hat{\phi}_{01}$ and $\hat{\phi}_{02}$ are given.

The numerical solution of the model will be presented in the next paper.

4. CONCLUSIONS

The presented results are based on the ontological model of the QQM and QFT, i.e., on the Cauchy continuum and the Planck unit cell concepts. The major progress is due to the

use of the quaternion algebra and some structurally symmetric quaternion formulas, specifically the postulate of quaternion velocity. It allows the consideration of the momentum of the expanding Cauchy continuum and is the apparent result of the scalar potential $\sigma_0(t, x)$ of the expansion/compression. This idea allows the formulation of the boundary conditions in the electron model. The key new results are listed below:

The quaternionic $G_0(m)(\sigma_0 + \hat{\phi})$, vectorial $G_0(m)\hat{\phi}$ and scalar: $G_0(m)\sigma_0$ propagators are postulated and used to generate the second order PDE systems for the proton, electron and neutron.

The scrupulous assessment of the second order PDE systems allows the postulation of two second order PDE systems for the *u* and *d* quarks from the *up* and *down* groups.

It is shown that both the proton and the neutron adhere to the experimental findings and are formed by three quarks. Namely, the proton and neutron are formed by *d*-*u*-*u* and *d* – *d* – *u* complexes, respectively. All the above PDE systems comply with the Cauchy equation of motion (16) and can be considered as stable particles.

The *u* and *d* quark systems do not comply with the Cauchy equation of motion. Also experimental efforts to find the individual quarks were without success. Observed were the bound states of the three quarks – the baryons and a quark and an antiquark – the mesons. Wilczek calls it the phenomenological paradox*: Quarks are Born Free, but Everywhere They are in Chains* [42]. The inconsistency of the quarks PDES with the Cauchy equation of motion elucidates the observed *Quarks Chains.*

The principle of special relativity is explained by this model and may well be applied for all practical purposes. The matter almost completely is built up by electromagnetic forces, so we must expect that both Lorentz contraction and time dilatations will be exactly as predicted by the Lorenz transformations. In the light of this prediction, it is unsurprising that the experiments by Michelson, Morley and many others did not reveal the speed of the Earth through the spatial continuum, which at that time was called the ether.

The results indicate the following targets for an immediate future:

- The particles and quarks in the case of higher coupling coefficients: $n \in \mathbb{Z}$, $n \neq 0$.
- The ratios between the constants for the different force fields.
- The rigorous derivation of the first order PDE basing on the extremum principle.

The multivalued coordinate transformation to determine the properties of space with curvature and torsion produced by the second order PDE systems representing the QFT [43].

FUNDING

This work was supported by the Faculty of Applied Mathematics AGH University of Krakow statutory tasks within the framework of a subsidy from the Ministry of Science and Higher Education, agreement no. 16.16.420.054.

ACKNOWLEDGEMENTS

The ideas reported here were developed during several discussions with Chantal Roth. Her criticisms and suggestions were useful in the present QQM formulation. We owe her our profound thanks.

APPENDIX

Symbols

$\hbar$	Planck constant in terms of angular frequency
$\mathbb{H}$	quaternion algebra
QFT	quaternion field theory
QQM	quaternion quantum mechanics
PDE	partial differential equation
$c = \frac{l_P}{t_P}$	transverse wave velocity in elastic continuum
$c_L = \sqrt{3}c$	longitudinal wave velocity in elastic continuum
f	frequency of the particle wave
$f_P = \frac{1}{t_P}$	Planck frequency, inverse of the Planck time
$G_0(m)$	frequency of the quaternionic oscillator
$G_0(m)\sigma \cdot \sigma^*$	scalar propagator I
$G_0(m)\sigma_0$	scalar propagator II
$G_0(m)\hat{\phi}$	vectorial propagator
$G_0(m)(\sigma_0 + \hat{\phi})$	quaternionic *q*-potential propagator
h	Planck constant, $h = 2\pi\hbar$
l_P	Planck length
m	equivalent mass of the wave, i.e., mass of the particle
m_P	Planck mass
N	coupling coefficient in the oscillator
T	deformation tensor
$\boldsymbol{u} = (u_1, u_2, u_3)$	displacement in $\mathbb{R}^3$
λ	length of the particle wave
λ, μ	Lamé coefficients
ρ	mass density of the particle $\rho = \rho_E/c^2$, as the equivalent of the energy density ρ_E in the PK-C
ρ_E	density of the deformation energy
$\rho_P = \frac{4m_P}{l_P^3}$	Planck density, i.e., the mass density of the PK-C
$\sigma = (\sigma_0, \phi_1, \phi_2, \phi_3)$	q-potential in $\mathbb{R}^4$, the quaternion deformation potential
σ'	stress tensors
$\sigma^* \cdot \sigma$	strain energy density
$\psi = \sigma\sqrt{\frac{\rho_P}{m}}$	quaternionic particle density, i.e., the particle wave function
$\psi \cdot \psi^*$	probability, i.e., the normalized particle mass density

REFERENCES

[1] von Neumann J. (1996). *Mathematische Grundlagen der Quantenmechanik*. Zweite Auflage. Berlin – Heidelberg – New York: Springer. DOI: https://doi.org/10.1007/978-3-642-61409-5.

[2] Birkhoff G. & von Neumann J. (1936). The logic of quantum mechanics. *Annals of Mathematics,* 37(4), 823–843. DOI: https://doi.org/10.48550/arXiv.2510.12502.

[3] Lanczos C. (1919). Die Funktionentheoretischen Beziehungen der Maxwellschen Æthergleichungen Ein Beitrag zur Relativitäts und Elektronentheorie, Verlagsbuchhandlung Josef Németh, Budapest. In: Davis W.R., Chu M.T., Dolan P., McConnell J.R., Norris L.K., Ortiz E., Plemmons R.J., Ridgeway D.,Scaife B.K.P., Stewart W.J., York J.W.Jr., Dogget W.O., Gellai B.M, Gsponer A.A. & Prioli C.A. (Eds.), *Cornelius Lanczos Collected Published Papers with Commentaries*, VI, Releigh, NC, USA: North Carolina State University, A1-A82.

[4] Lanczos C. (1932). Electricity as a natural property of Riemannian geometry. *Physical Review*, 39(4), 716–736. DOI: https://doi.org/10.1103/PhysRev.39.716.

[5] Lanczos C. (1933). Die Wellenmechanik als Hamiltonsche Dynamik des Funktionraumes. Eine neue Ableitung der Diracschen Gleichung. *Zeitschrift für Physik*, 81, 703–732, DOI: https://doi.org/10.1007/BF01342068.

[6] Fueter R. (1935). The Funktionentheorie der Differentialgleichungen $\Delta u = 0$ und $\Delta\Delta u = 0$ mit vier reellen Variablen. *Commentarii Mathematici Helvetici*, 7, 307–330. URL: http://eudml.org/doc/138642.

[7] Adler S.L. (1996). Quaternionic quantum mechanics and noncommutative dynamics. DOI: https://doi.org/10.48550/arXiv.hep-th/9607008.

[8] Christianto V. (2006). A new wave quantum relativistic equation from quaternionic representation of Maxwell–Dirac equation as an alternative to Barut–Dirac equation. *Electronic Journal of Theoretical Physics*, 3 (12), 117–144. URL: https://vixra.org/pdf/1411.0300v1.pdf.

[9] Harari H. (1979). A schematic model of quarks and leptons. *Physics Letters B*, 86(1), 83–86. DOI: https://doi.org/10.1016/0370-2693(79)90626-9.

[10] Adler S.L. (1994). Composite leptons and quarks constructed as triply occupied quasiparticles in quaternionic quantum mechanics*. Physics Letters B*, 332(3–4), 358–365*.* DOI: https://doi.org/10.1016/0370-2693(94)91265-3.

[11] Horwitz L.P. & Biedenharn L.C. (1984). Quaternion quantum mechanics: Second quantization and gauge fields. *Annals of Physics*, 157(2), 432–488. DOI: https://doi.org/10.1016/0003-4916(84)90068-X.

[12] Adler S.L. (1995). Quaternionic quantum mechanics and quantum fields. Oxford: Oxford University Press. DOI: https://doi.org/10.1093/oso/9780195066432.001.0001.

[13] Arbab A. (2011). The quaternionic quantum mechanics *Applied Physics Research*, 3(2), 160-170. DOI: https://doi.org/10.5539/apr.v3n2p160.

[14] Arbab A. & Al Ajmi M. (2018). The quaternioning commutator bracket and its implications. *Symmetry*, 10(10), 513. DOI: https://doi.org/10.3390/sym10100513.

[15] Giardino S. (2025). Self-interacting quantum particles. *International Journal of Geometric Methods in Modern Physics*, 22(12), 2550088. DOI: https://doi.org/10.1142/S0219887825500884.

[16] Giardino S. (2023). Generalized imaginary units in quantum mechanics. URL: https://arXiv:2311.14162.

[17] Danielewski M. (2007). The Planck–Kleinert Crystal. *Zeitschrift für Naturforschung A*, 62(10–11), 564–568. DOI: https://doi.org/10.1515/zna-2007-10-1102.

[18] Danielewski M. & Sapa L. (2020). Foundations of the quaternion quantum mechanics. *Entropy,* 22(12), 1424, 14–24. DOI: https://doi.org/10.3390/e22121424.

[19] Danielewski M. & Sapa L. (2017). Nonlinear Klein–Gordon equation in Cauchy–Navier elastic solid. *Вісник Черкаського університету. Серія: Фізико-математичні науки,* 1, 22–29.

[20] Danielewski M. (2022). An ontological basis for the diffusion theory. *Journal of Phase Equilibria and Diffusion*, 43, 883–893. DOI: https://doi.org/10.1007/s11669-022-01006-y.

[21] Danielewski M., Sapa L. & Roth Ch. (2023). Quaternion quantum mechanics II: Resolving the problems of gravity and imaginary numbers. *Symmetry*, 15(9), 1672. DOI: https://doi.org/10.3390/sym15091672.

[22] Başkal S., Kim Y.S. & Noz M.E. (2015) *Physics of the Lorentz Group.* San Rafael, CA, USA: Morgan & Claypool Publishers. DOI: https://doi.org/10.1088/978-1-6817-4254-0.

[23] Gürlebeck K. & Sprössig W. (1997). *Quaternionic and Clifford Calculus for Physicists and Engineers*; *Mathematical Methods in Practice*. New York: Wiley.

[24] Altmann S.L. (1986). *Rotations, Quaternions, and Double Groups*. New York: Clarendon Press.

[25] Graves R.P. (1989). *Life of Sir William Rowan Hamilton.* Dublin: Hodges, Figgis & Co.

[26] Gürlebeck K. & Sprössig W. (1989) *Quaternionic Analysis and Elliptic Boundary Value Problems*. Berlin: Akademie-Verlag. DOI: https://doi.org/10.1002/zamm.19920720117.

[27] Cauchy A.L. (1823). Récherches sur L'équilibre et le Mouvement Intérieur des Corps Solides ou Fluides, Élastiques ou non Élastiques. *Bulletin de la Société Philomathique de Paris*, 9, 300–304.

[28] Poisson D. (1829). Mémoire sur L'équilibre et le Mouvement des Corps Élastiques. *Mémoires de l'Académie des Sciences de Paris*, 8, 357–570.

[29] Neumann F. (1885). *Vorlesungen über die Theorie der Elasticität der Festen Körper und des Lichtäthers*. Leipzig: B.G. Teubner.

[30] Duhem P. (1899). Sur l'intégrale des équations des petits mouvements d'un solide isotrope. *Mémoires de la Société des Sciences de Bordeaux*, Ser. V, t. III, 317– 329.

[31] Love A.E.H. (1944). *Mathematical Theory of Elasticity,* 4th Edition. New York: Dover Publications Inc.

[32] Marder M.P. (2000). *Condensed Matter Physics*. New York: John Wiley & Sons.

[33] Landau L.D. & Lifshitz E.M. (1986). *Theory of Elasticity*, 3rd Edition. Amsterdam: Butterworth-Heinemann Elsevier Ltd.

[34] National Institute of Standards and Technology (2018). URL: https://www.nist.gov/physics.

[35] Feynman R. (1963). *The Feynman Lectures in Physics*, Vol. 1. Boston: Addison-Wesley Publishing Co.

[36] Glötzl E. & Richters E.O. (2023). Helmholtz decomposition and potential functions for n-dimensional analytic vector fields. *Journal of Mathematical Analysis and Applications*, 525(2), 127–138. DOI: https://doi.org/10.1016/j.jmaa.2023.127138.

[37] Bodurov T. (1988). Generalized Ehrenfest theorem for nonlinear Schrödinger equations. *International Journal of Theoretical Physics*, 37, 1299–1306. DOI: https://doi.org/10.1023/A:1026632006040.

[38] Zeidler E. (1990). *Nonlinear Functional Analysis and Its Applications II/A: Linear Monotone Operators*. New York: Springer. DOI: https://doi.org/10.1007/978-1-4612-0985-0.

[39] Dirac P.A.M. (1952). Is there an aether? *Nature,* 168(4282), 906–907.

[40] Reid C. (1969). *Hilbert*. Berlin: Springer-Verlag.

[41] Derbes D. (1996). Feynman's derivation of the Schrödinger equation. *American Journal of Physics*, 64(7), 881–884. URL: https://web.physics.utah.edu/~starykh/phys7640/Lectures/FeynmansDerivation.pdf.

[42] Wilczek F. (2005). Nobel lecture: Asymptotic freedom: from paradox to paradigm. *Reviews of Modern Physics*, 77(3), 857–870. DOI: https://doi.org/10.1103/RevModPhys.77.857.

[43] Kleinert H. (1989). *Gauge Fields in Condensed Matter, Vol. II, Stresses and Defects*. Singapore: World Scientific, Singapore. URL: https://hagenkleinert.de/documents/gf/HagenKleinert_GaugeFieldsInCondensedMatter_Part3.pdf.